Determination of the intermolecular potential energy surface for $(HCl)_2$ from vibration–rotation–tunneling spectra

M. J. Elrod[a] and R. J. Saykally
Department of Chemistry, University of California, Berkeley, California 94720

(Received 26 October 1994; accepted 5 April 1995)

An accurate and detailed semiempirical intermolecular potential energy surface for $(HCl)_2$ has been determined by a direct nonlinear least-squares fit to 33 microwave, far-infrared and near-infrared spectroscopic quantities using the analytical potential model of Bunker *et al.* [J. Mol. Spectrosc. **146**, 200 (1991)] and a rigorous four-dimensional dynamical method (described in the accompanying paper). The global minimum ($D_e=-692$ cm^{-1}) is located near the hydrogen-bonded L-shaped geometry ($R=3.746$ Å, $\theta_1=9°$, $\theta_2=89.8°$, and $\phi=180°$). The marked influence of anisotropic repulsive forces is evidenced in the radial dependence of the donor–acceptor interchange tunneling pathway. The minimum energy pathway in this low barrier (48 cm^{-1}) process involves a contraction of 0.1 Å in the center of mass distance (R) at the C_{2h} symmetry barrier position. The new surface is much more accurate than either the *ab initio* formulation of Bunker *et al.* or a previous semiempirical surface [J. Chem. Phys. **78**, 6841 (1983)]. © *1995 American Institute of Physics.*

I. INTRODUCTION

During the past decade, the investigation of intermolecular forces via the study of van der Waals complexes has been greatly advanced by progress in both high resolution molecular spectroscopy techniques and the complementary theoretical methods required to calculate the spectrum from a trial intermolecular potential energy surface. In favorable situations, it has been possible to determine *experimental* potential energy surfaces by directly fitting spectroscopic data to detailed analytical models of the intermolecular interactions.[1] In order to invert spectroscopic data to obtain a potential surface in this fashion, it is necessary to solve the associated multidimensional intermolecular dynamics problem very accurately and efficiently such that the calculation of the relevant eigenvalues and eigenvectors can be placed inside of a least-squares fitting loop. The various methods currently in use for this purpose are summarized in recent reviews.[2,3] Principally due to limitations in these computational techniques (and available computers), the systems for which such calculations have been used in conjunction with least-squares fitting of high precision spectroscopic data to determine improved intermolecular potential surfaces (IPS) have been limited to (1) rare gas (R_g) pairs[4] (one intermolecular degree of freedom), (2) Rg–H_2 systems,[5–7] and Rg–hydrogen halides[8] (two intermolecular degrees of freedom), and (3) Ar–H_2O,[9] and Ar–NH_3 (Ref. 10) (three intermolecular degrees of freedom). Quack and Suhm[11] have obtained several six-dimensional (including chemical bond stretch) semiempirical IPS for the HF dimer system through fitting of *ab initio* points to an analytical model, then adjusting various terms in the model to force agreement with several known properties of the dimer (dissociation energy, F—F bond distance, rotational constant) with the use of quantum Monte Carlo (QMC) methods. Most recently, an empirical six-dimensional intermolecular potential for $(NH_3)_2$ has been constructed by van der Avoird *et al.* which impressively reproduces many of the measured spectroscopic properties.[12] However, since the latter two studies did not employ direct least-squares fitting of the data, the reliability of these potential surfaces for $(NH_3)_2$ and $(HF)_2$ is not really comparable to the simpler IPS listed above.

The new direction addressed in the present work is the extension of the direct least-squares fitting methods to the determination of interaction potentials that are of genuine chemical significance. All of the existing rigorously determined potential surfaces involve rare gas atoms and, although these systems provide important benchmarks and paradigms, these results are not generalizable to the more strongly interacting molecular systems. The simplest molecular system from the point of view of intermolecular dynamics is that of a pair of linear molecules, which constitutes a four-dimensional intermolecular dynamics problem (the coordinate system is depicted in Fig. 1). In particular, we address appropriate theoretical techniques for precisely calculating the vibration–rotation–tunneling (VRT) spectra of the $(HCl)_2$ complex in the accompanying paper (which will be referred to as I),[13] and we turn here to a general discussion of this system.

Because hydrogen chloride is a prototypical hydrogen-bonding system, its condensed phases have been the subject of extensive experimental investigation through dielectric properties,[14] and nuclear magnetic resonance,[15,16] infrared and Raman,[17–23] spectroscopies, and x-ray and neutron diffraction techniques.[24–27] More recently, the HCl intermolecular interaction has been investigated with gas phase experimental techniques. The $(HCl)_2$ complex was initially characterized by unresolved vibrational structure in the infrared spectrum of the HCl monomer by Rank and co-workers.[28,29] In a related development, Dyke *et al.*[30] used high resolution molecular beam electric resonance techniques in a study of $(HF)_2$, and found that although the

[a]Present address: Department of Earth, Atmospheric, and Planetary Sciences, Massachusetts Institute of Technology, 54-1312, Cambridge, MA 02139.

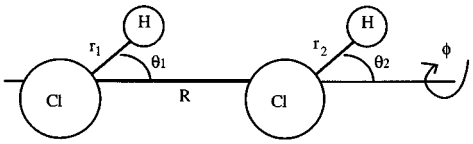

FIG. 1. Coordinate system for $(HCl)_2$. The "L-shaped" equilibrium structure determined in this work occurs at $\theta_1=9°$, $\theta_2=89.8°$, $\phi=180°$, and $R=3.746$ Å. The monomer bond lengths (r_1 and r_2) were fixed at their equilibrium values (2.412 a.u.).

hydrogen-bonded equilibrium structure was an L-shaped configuration, quantum tunneling rapidly interchanges the roles of the hydrogen bond donor and acceptor. This tunneling motion results in the splitting of each rotational level into a symmetric and antisymmetric component, with the selection rules requiring that the transitions result in a change in the tunneling state symmetry. Since the tunneling splitting provides a very sensitive characterization of the height and shape of the barrier to donor–acceptor interchange, these data provide crucial information on the intermolecular potential energy surface, which is the feature of ultimate interest. Although extensive high resolution infrared studies of $(HCl)_2$ were later carried out[31] as well as coherent anti-Stokes Raman spectroscopy (CARS),[32] similar measurements of the tunneling splitting for $(HCl)_2$ remained elusive. In the late 1980s, far-infrared laser spectroscopy measurements of the $K_a=0\rightarrow1$ tunneling subband[33] and near-infrared measurements of the tunneling splitting for the mixed dimer $(H^{35}Cl–H^{37}Cl)$[34] finally led to the direct measurement of the ground state tunneling splitting by far-infrared laser techniques.[35] Since that time, Fourier-transform far-infrared techniques have been used to measure several rotation–tunneling subbands associated with the intermolecular out-of-plane bending vibration,[36] and Schuder *et al.* recently reported extensive near-infrared measurements for $(HCl)_2$ (Ref. 37) and $(DCl)_2$.[38]

The extensive theoretical efforts in the study of the HCl–HCl interaction can roughly be divided into *ab initio* investigations, semiempirical methods which emphasize condensed phase properties, and the calculation of spectra designed to test proposed potential energy surfaces (including *ab initio* models). Although most of the previous *ab initio* calculations were performed at the self-consistent field (SCF) level,[39–42] there have been several recent studies which included the influence of electron correlation.[43–45] Other *ab initio* calculations have also been carried out at lower levels of theory to facilitate a global mapping of the four-dimensional IPS (see Fig. 1).[46–48] These potentials were then used in molecular dynamics simulations of liquid HCl and subsequently refined to yield more accurate semiempirical surfaces. In particular, the work of Votava *et al.*[48] is notable in that both radial distribution functions obtained from neutron scattering from liquid HCl[27] and experimental second virial coefficients[49] were used to refine the potential. In a study vital to the present work, Karpfen *et al.*[50] determined the $(HCl)_2$ potential surface at 1654 geometries via relatively high level *ab initio* calculations. Bunker *et al.*[51] subsequently fit a six-dimensional analytical function (cast in a single center spherical expansion) through these points. Jensen *et al.*[52] used this analytical function in a full four-dimensional close-coupling calculation (only the high frequency intramolecular modes neglected) of the lowest intermolecular vibrational levels of $(HCl)_2$ in an attempt to evaluate the quality of the *ab initio* analytical potential by comparing to existing experimental spectra and to predict unobserved spectra. Because these calculations only included states with total angular momentum of zero, much of the existing experimental data could not actually be directly compared with the calculated results. In order to address this deficiency, Althorpe *et al.*[53] performed approximate three-dimensional calculations (radial coordinate fixed—"reversed adiabatic approximation") for total angular momentum values of up to two using the analytical *ab initio* potential, as well as an electrostatic potential surface based on only the dipole and quadrupole moment of HCl. Although the agreement between these potentials and the experimental spectra was not quantitative, the relative success of the simple electrostatic potential suggested that all of the essential anisotropy in the total IPS was indeed contained in the long-range attractive terms. We show in this paper, that such is not the case.

In an early attempt to deduce an experimental potential for $(HF)_2$, Barton and Howard[54] used the BOARS approximation[55] (separation of the radial and angular degrees of freedom) to calculate $(HF)_2$ spectra and to directly fit (via least-squares methods) a very simple low-order anisotropic repulsion+electrostatic potential energy surface. This approximation—which also reduces the maximum dimensionality of the problem to three—is also not sufficiently quantitative for the fitting of high resolution spectra for $(HF)_2$. However, the nature of the experimental data available at the time—which included only eigenstates located very near the bottom of the potential well—is the main limitation in the reliability of this IPS for $(HF)_2$. It should be emphasized, however, that this work represents the only previous attempt to directly fit a set of spectroscopic data to a flexible potential surface for a four-dimensional system—albeit with an approximate dynamical method and a quite crude potential model. In contrast, the $(HF)_2$ potential determination of Quack and Suhm[11] did not involve such a least-squares fit of the extensive spectroscopic data that exist (see references given in Ref. 11).

In this paper, we report the measurement of new far-infrared VRT spectra for $(HCl)_2$ and $(DCl)_2$ which access excited states in the tunneling coordinate, thus providing important new constraints on the form of the IPS—particularly with respect to the barrier to donor–acceptor interchange. Using a rigorous four-dimensional quantum dynamics technique to precisely calculate the spectroscopic observables (described in the accompanying paper), the best *ab initio* and semiempirical potential energy surfaces are evaluated by comparison to all new and existing experimental spectra. Finally, we describe the determination of a highly accurate experimental potential surface from a least-squares fit of the complete spectroscopic data set for $(HCl)_2$ and $(DCl)_2$ using a fully coupled four-dimensional dynamics method and a detailed intermolecular potential model.

II. EXPERIMENT

The new VRT spectra reported here were observed in a continuous supersonic planar jet expansion probed by a tunable far-infrared laser spectrometer. The spectrometer has been described in detail previously.[56,57] The tunable far-infrared radiation is generated by mixing an optically pumped line-tunable far-infrared gas laser with continuously tunable frequency modulated microwaves in a Schottky barrier diode to generate light at the sum and difference frequencies ($\nu=\nu_{\mathrm{FIR}}\pm\nu_{\mathrm{MW}}$). The tunable radiation is separated from the much stronger fixed frequency radiation with a Michelson polarizing interferometer and is then directed to a multipass cell which encloses the supersonic expansion. After passing ~10 times through the expansion, the radiation is detected by a Putley-mode InSb detector and the signal is demodulated at 2 f by a lock-in amplifier. Technical grade HCl (99.0%, Matheson) was used, and DCl was synthesized by reaction of D_2O with benzoyl chloride,[58] cryogenically distilled with liquid nitrogen and used with no further purification. $[H(D)Cl]_2$ was produced by continuously expanding a 1%–5% H(D)Cl (>5% was found to be optimal) in argon mixture at a stagnation pressure of 2 atm through a 10 cm by 25 μm planar jet into a vacuum chamber pumped by a 1200 ℓ/s Roots pump. The 939.494 GHz (CH_3OD), 980.5914 GHz (CH_3OD), 1101.1594 GHz (CH_2DOH), 1145.4305 GHz (CH_2F_2), and 1193.7273 GHz (CH_3OH) laser lines provided the fixed frequency far-infrared radiation. The signal strength for all of the transitions was found to be sensitive to the conditions of the molecular beam. The assignment of the spectra revealed that, despite the estimated rotational temperature of 5 K, all of the spectra observed originated from states 5 to 15 cm^{-1} above their respective ground states. A representative rotational feature of the spectrum (with resolved nuclear quadrupole hyperfine structure due to the spin $I=3/2$ chlorine nuclei) is shown in Fig. 2.

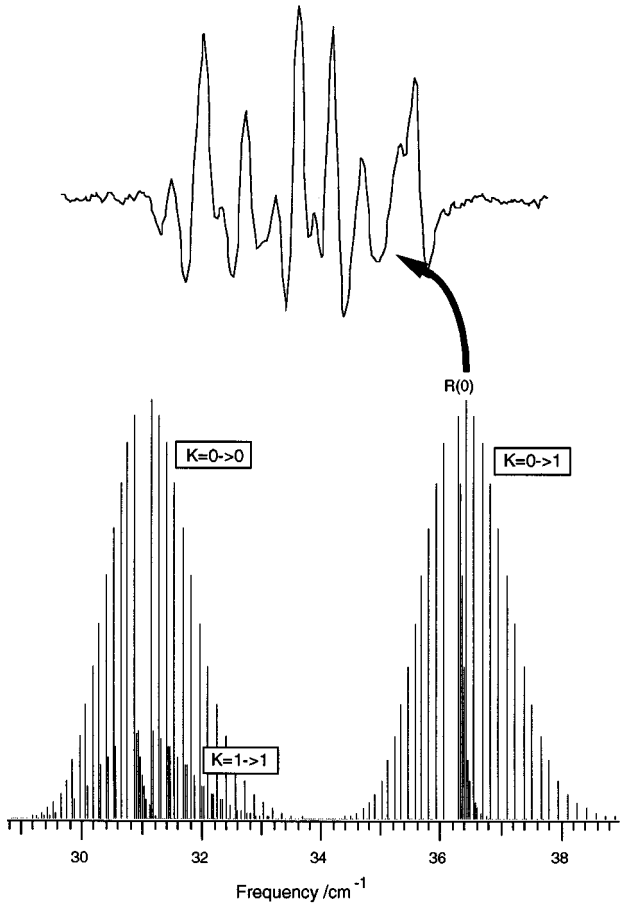

FIG. 2. Experimental spectrum for the $\nu_5=1\rightarrow2$ $K_a=0\rightarrow1$ $J=0\rightarrow1$ $(DCl)_2$ transition. The structure shown in the $R(0)$ line is due to the $I=3/2$ quadrupole interactions of the chlorine nuclei.

III. DATA ANALYSIS

For the purposes of discussing the spectroscopic energy levels of $(HCl)_2$, it is necessary to adopt a notation to describe the intra- and intermolecular vibrations of the complex. The intermolecular eigenstates are labeled with the following notation: $|\nu_3\nu_4\nu_5\nu_6\rangle$. The high frequency HCl stretching modes are denoted ν_1 and ν_2, for the ''free'' and ''bound'' monomers, respectively. For the intermolecular modes, the in-plane ''antigeared'' bending vibration is denoted ν_3, the intermonomer Cl–Cl stretch is denoted ν_4, the in-plane ''geared'' bend is denoted ν_5, and the out-of-plane bend is denoted ν_6. The ν_5 mode correlates with the preferred tunneling path, and the $\nu_5=0\rightarrow1$ energy difference can be identified as the tunneling splitting due to the permutation symmetry of the dimer. An energy level diagram for $(HCl)_2$ is shown in Paper I. It is also useful to classify the vibration–rotation–tunneling (VRT) levels according to their irreducible representations in the $C_{2h}(M)$ molecular symmetry group. The electric dipole selection rules require $A\leftrightarrow A$ or $B\leftrightarrow B$ and $+\leftrightarrow-$. The A/B rule is responsible for the previously mentioned requirement that transitions result in a change in the tunneling state symmetry. This result, and the large tunneling splitting account for the result that $(HCl)_2$ has no allowed transitions in the microwave region, unlike the case of $(HF)_2$.

The $\nu_5=1\rightarrow2$ $K_a=0\rightarrow0$ subbands for $(H^{35}Cl)_2$, $(H^{35}Cl)(H^{37}Cl)$, $(D^{35}Cl)_2$, and $(D^{35}Cl)(D^{37}Cl)$, the $\nu_5=1\rightarrow2$ $K_a=1\rightarrow1$ subbands for $(D^{35}Cl)_2$, and $(D^{35}Cl)(D^{37}Cl)$, and the $\nu_5=1\rightarrow2$ $K_a=0\rightarrow1$ subbands for $(D^{35}Cl)_2$, and $(D^{35}Cl)(D^{37}Cl)$ were recorded with full rotational and partial hyperfine resolution. Following the established convention for $(HCl)_2$ and $(HF)_2$,[36] the hyperfine-free line centers were fit to a model that allows each K_a manifold to possess its own set of rotational parameters. In addition, because $(HCl)_2$ is a very near prolate asymmetric top, the asymmetry splitting can be treated perturbatively. We used the expression

$$E_{K_a}=\nu_{K_a}+(1/2)(B_{K_a}+C_{K_a})J(J+1)-D_{K_a}[J(J+1)-K_a^2]^2\pm\Delta E_{K_a}, \quad (1)$$

where ΔE_{K_a} is the asymmetry splitting

$$\Delta E_{K_a}=(1/4)(B_{K_a}-C_{K_a})J(J+1) \quad (2)$$

for states where $K_a=1$. We are also able to determine A_{eff} (defined as the difference between the real or virtual $J=0$

TABLE I. Spectroscopic constants[a] (1σ uncertainties in parentheses) for $(HCl)_2$.

$\lvert\nu_3\nu_4\nu_5\nu_6\rangle$	K_a	Parameter	$(H^{35}Cl)_2$	$(H^{35}Cl)(H^{37}Cl)$
$\lvert0\,0\,1\,0\rangle$	0	$(B+C)/2$ (MHz)	1915.071(18)	1864.56(3)
		D_J (kHz)	8.2(3)	6.9(7)
		$\langle P_2(\cos\theta)\rangle^{35}$	0.187(6)	0.187[b]
		$\langle P_2(\cos\theta)\rangle^{37}$		0.191(6)
		$\nu_5=2\leftarrow1$ (cm^{-1})	37.645 395(3)	37.298 817(6)
$\lvert0\,0\,2\,0\rangle$	0	$(B+C)/2$ (MHz)	1923.984(18)	1872.60(2)
		D_J (kHz)	10.1(2)	9.0(7)
		$\langle P_2(\cos\theta)\rangle^{35}$	0.179(8)	0.179[b]
		$\langle P_2(\cos\theta)\rangle^{37}$		0.186(17)

[a]Observed transition frequencies available on request from authors.
[b]Fixed to value for $(H^{35}Cl)_2$.

states of $K_a=0$ and $K_a=1$ for a given vibrational level) for $(DCl)_2$ because both parallel and perpendicular transitions were measured connecting the $K_a=0$ and $K_a=1$ levels in both vibrational states. The spectroscopic constants for $(HCl)_2$ are contained in Table I and for $(DCl)_2$ in Table II. The fitted rotational constants confirm $\nu_5=1$ (the first excited ''tunneling'' state) as the lower state for all of the new transitions reported here for $(HCl)_2$ and $(DCl)_2$.

The nuclear quadrupole hyperfine structure was fit to energies obtained from a Hamiltonian appropriate for a two-spin system. The following angular momentum coupling scheme was used:

$$\mathbf{I_1}+\mathbf{I_2}=\mathbf{I}, \quad \mathbf{I}+\mathbf{J}=\mathbf{F}. \tag{3}$$

The matrix elements are evaluated in a symmetric top basis,[59]

TABLE II. Spectroscopic constants[a] (1σ uncertainties in parentheses) for $(DCl)_2$.

$\lvert\nu_3\nu_4\nu_5\nu_6\rangle$	K_a	Parameter	$(D^{35}Cl)_2$	$(D^{35}Cl)(D^{37}Cl)$
$\lvert0\,0\,1\,0\rangle$	0	$(B+C)/2$ (MHz)	1896.27(3)	1846.98(4)
		D_J (kHz)	8.2(6)	6.7(10)
		$\langle P_2(\cos\theta)\rangle^{35}$	0.189(5)	0.189[b]
		$\langle P_2(\cos\theta)\rangle^{37}$		0.20(2)
		$\nu_5=2\leftarrow1$ (cm^{-1})	31.012 263(10)	30.955 251(13)
$\lvert0\,0\,2\,0\rangle$	0	$(B+C)/2$ (MHz)	1929.85(4)	1879.48(4)
		D_J (kHz)	7.6(5)	6.4(9)
		$\langle P_2(\cos\theta)\rangle^{35}$	0.193(8)	0.193[b]
		$\langle P_2(\cos\theta)\rangle^{37}$		0.19(3)
$\lvert0\,0\,1\,0\rangle$	1	$(B+C)/2$ (MHz)	1896.03(3)	1846.86(4)
		$(B-C)$ (MHz)	27.77(5)	26.37(7)
		A_{eff} (cm^{-1})	5.386 162(13)	5.380 828(15)
		D_J (kHz)	7.8(5)	5.2(11)
$\lvert0\,0\,2\,0\rangle$	1	$(B+C)/2$ (MHz)	1931.74(3)	1881.32(3)
		$(B-C)$ (MHz)	35.81(4)	34.00(6)
		A_{eff} (cm^{-1})	5.291 146(13)	5.287 334(15)
		D_J (kHz)	7.3(4)	6.4(9)

[a]Observed transition frequencies available on request from authors.
[b]Fixed to value for $(D^{35}Cl)_2$.

$$\begin{aligned}
&\langle I_1 I_2 IJKFM_F|H_Q|I_1 I_2 I'J'K'F'M_F'\rangle \\
&= \delta_{FF'}\delta_{M_F M_F'}\frac{(-1)^{(I'+I_1+I_2+F+K)}}{4}[(2I+1)(2I'+1) \\
&\times(2J+1)(2J'+1)]^{1/2}\begin{Bmatrix} I & I' & 2 \\ J' & J & F \end{Bmatrix} \\
&\times\begin{pmatrix} J & 2 & J' \\ -K & -q & K' \end{pmatrix}\Bigg[(-1)^{I'}\frac{\begin{Bmatrix} I & I' & 2 \\ I_1 & I_1 & I_2 \end{Bmatrix}}{\begin{pmatrix} I_1 & 2 & I_1 \\ -I_1 & 0 & I_1 \end{pmatrix}} \\
&\times(\chi_{2-q})_1+(-1)^{I}\frac{\begin{Bmatrix} I & I' & 2 \\ I_2 & I_2 & I_1 \end{Bmatrix}}{\begin{pmatrix} I_2 & 2 & I_2 \\ -I_2 & 0 & I_2 \end{pmatrix}}(\chi_{2-q})_2\Bigg],
\end{aligned} \tag{4}$$

where the quantities in parentheses and braces are 3-j and 6-j symbols, respectively, and the nuclear quadrupole coupling constants, χ_{2-q}, can be related to the usual Cartesian components by

$$\chi_{20}=\chi_{aa}, \tag{5}$$

$$\chi_{2\pm1}=(2/3)^{1/2}\chi_{ab}, \tag{6}$$

and

$$\chi_{2\pm2}=(1/6)^{1/2}(\chi_{bb}-\chi_{cc}). \tag{7}$$

Only first-order energies ($\Delta J=0$ and $\Delta K=0$) were evaluated for the purposes of fitting the experimental spectra. The value of $\langle P_2(\cos\theta)\rangle$ is reported rather than χ_{aa}, since that quantity $[\langle P_2(\cos\theta)\rangle=\chi_{aa}/\chi_{\text{HCl}}]$ is more directly related to the angular orientation of the HCl monomers within the complex. These quantities are reported in Tables I and II for $(HCl)_2$ and $(DCl)_2$, respectively.

IV. ANALYTICAL INTERMOLECULAR POTENTIAL ENERGY SURFACES FOR $(HCl)_2$

In 1983, Votava *et al.*[48] performed *ab initio* calculations (electron correlation included at the CEPA-1-SD level) on $(HCl)_2$ in order to construct an analytical potential energy surface for the purposes of performing molecular dynamics calculations on liquid HCl. The *ab initio* points were fit to an effective three point-charge model [at the positions of the hydrogen atom (charge +0.403 a.u.), chlorine atom (charge −0.909 a.u.), and a dummy center (charge 0.506 a.u.) positioned outside the molecule on the side of the chlorine atom] with exp-6 functions between H–Cl and Cl–Cl sites and angle-dependent H–H exponential repulsion. This model was refined so that agreement with experimental second virial coefficients and experimental liquid properties (radial distribution functions) was improved. Since this semiempirical potential energy surface continues to be employed in modern studies of HCl,[60] it is important to test the quality of this potential with respect to the results from spectroscopy. This is described later in the paper.

In 1991, Bunker *et al.*[51] determined an *ab initio* six-dimensional (including both HCl monomer stretching motions) analytical potential energy surface for $(HCl)_2$ from the earlier calculations of Karpfen *et al.*[50] by fitting the potential points to an elaborate, accurate single-center spherical expansion form

$$V(r_1,r_2,R,\theta_1,\theta_2,\phi) = \sum_{l_1 l_2 l} A_{l_1 l_2 l}(R,r_1,r_2) g_{l_1 l_2 l}(\theta_1,\theta_2,\phi) + V_{\text{short range}}. \tag{8}$$

Here the angular basis set for the expansion is defined as

$$g_{l_1 l_2 l}(\theta_1,\theta_2,\phi) = (-1)^{l_1-l_2} \frac{2l+1}{2\pi^{1/2}} \left\{ \begin{pmatrix} l_1 & l_2 & l \\ 0 & 0 & 0 \end{pmatrix} P_{l_1 0}(\theta_1) P_{l_2 0}(\theta_2) + \sum_{m=1}^{l_m} (-1)^m 2 \begin{pmatrix} l_1 & l_2 & l \\ m & -m & 0 \end{pmatrix} P_{l_1 m}(\theta_1) P_{l_2 m}(\theta_2) \cos(m\phi) \right\}, \tag{9}$$

and where, in turn, the symbols in parentheses are $3-j$ symbols, l_m is the smaller of l_1 and l_2, and $P_{lm}(\theta)$ is an unnormalized associated Legendre function related to the spherical harmonic functions by

$$Y_{lm}(\theta,\phi) = P_{lm}(\theta)\exp(im\phi). \tag{10}$$

The very short-range repulsion (for geometries where the atoms begin to overlap) is separately parametrized,

$$\begin{aligned} V_{\text{short range}} = [& a \exp(-2.5R_{12})\eta^-(2.0,4.0;R_{12}) \\ & + b \exp(-3R_{14})\eta^-(2.0,4.0;R_{14}) \\ & + b \exp(-3R_{23})\eta^-(2.0,4.0;R_{23})] \\ & \times \eta^-(2.0,3.5;r_1)\eta^-(2.0,3.5;r_2), \end{aligned} \tag{11}$$

and damped out at long range by the following functions:

$$\eta^{\pm}(t,u;R) = 0.5\{1 \pm \tanh[t(R-u)]\}. \tag{12}$$

The very short-range repulsion can be entirely neglected in calculations of bound intermolecular states since the wave functions for those states do not possess significant amplitude in the region of the potential where the short-range term is significant. Because of the invariance of the potential under the Eq. (12) permutation operation, the $A_{l_1 l_2 l}(R,r_1,r_2)$ coefficients are related by

$$A_{l_1 l_2 l}(R,r_1,r_2) = (-1)^{l_1+l_2} A_{l_2 l_1 l}(R,r_2,r_1). \tag{13}$$

In addition, the invariance of the potential under the E^* operation requires

$$(-1)^{l_1+l_2+l} = 1. \tag{14}$$

The expression for A_{000} is given by

$$\begin{aligned} A_{000} = & k_0^{000} + [k_1^{\text{sr}} \exp(-d_3) + k_2^{\text{sr}} \exp(-2d_3)] \\ & \times \eta^-(2.0,6.0;R) + [k_1^{000} \exp(-d_3) + k_2^{000} \\ & \times \exp(-2d_3)]\eta^+(2.0,6.0;R)\eta^-(0.5,8.5;R) \\ & + \frac{k_6^{000}}{R^6} \eta^+(2.0,6.0;R) + k_{11}^{000}(y_1^2+y_2^2), \end{aligned} \tag{15}$$

where

$$y_1 = 1 - \exp(-c_3 d_1), \tag{16}$$

$$y_2 = 1 - \exp(-c_3 d_2), \tag{17}$$

$$d_1 = r_1 - c_1, \tag{18}$$

$$d_2 = r_2 - c_1, \tag{19}$$

and

$$d_3 = R - c_2, \tag{20}$$

and where c_1, c_2, and c_3 are adjustable parameters. The expression for other $A_{l_1 l_2 l}(R,r_1,r_2)$ is

$$\begin{aligned} A_{l_1 l_2 l} = & [k_1^{l_1 l_2 l} \exp(-d_3) + k_2^{l_1 l_2 l} \exp(-2d_3) \\ & + k_3^{l_1 l_2 l} \exp(-3d_3) + k_4^{l_1 l_2 l} \exp(-4d_3) \\ & + k_5^{l_1 l_2 l} \exp(-5d_3) + k_9^{l_1 l_2 l} y_1 \\ & + k_{10}^{l_1 l_2 l} y_2]\eta^+(2.0,6.0;R)\eta^-(0.5,8.5;R) \\ & + \left[\frac{k_6^{l_1 l_2 l}}{R^6} + \frac{k_7^{l_1 l_2 l}}{R^7} + \frac{k_8^{l_1 l_2 l}}{R^8} \right] \eta^+(2.0,6.0;R). \end{aligned} \tag{21}$$

In addition, the electrostatic contribution to each of the $l_1+l_2=l$ terms was added to give the potential correct long-range behavior

$$A_{l_1 l_2 l}^{\text{elec}} = (-1)^{l_2} 8\pi^{3/2} \delta_{(l_1+l_2),l} \times \left(\frac{(2l_1+1)!}{(2l+1)(2l_1+1)!(2l_2+1)!} \right)^{1/2} \frac{Q_{l_1} Q_{l_2}}{R^{l+1}}, \tag{22}$$

where Q_l are the HCl multipole moments. The dipole, quadrupole, and octupole moments were held fixed at the *ab initio* values and the $l=4$ and $l=5$ moments were adjustable parameters. The damping functions (η) were used to damp out

the electrostatic terms for R less than $6a_0$, to ensure that the only anisotropic terms at distances greater than $8.5a_0$ are those of electrostatic or dispersion, and that only the k_0^{000}, k_6^{000}, and k_{11}^{000} isotropic terms extend to R greater than $8.5a_0$. This potential did not explicitly include induction effects, which are known to be very small.[51]

This detailed expression was fit to the 1654 *ab initio* points using 38 (27 pertaining to the four-dimensional intermolecular potential) variable parameters. The analytical potential minimum was found to be -626 cm^{-1} at $r_1=r_2=1.278$ Å, $R=3.82$ Å, $\theta_1=7.4°$, $\theta_2=87.7°$, $\phi=180°$, in good agreement with the pure *ab initio* minimum. The standard deviation of the fit was 19 cm^{-1}, although the analytical surface produces more accurate energies near the potential minimum. It should be noted that the quality of the analytical fit—in addition to the quality of the *ab initio* calculation itself—is a determining factor in the ultimate accuracy of this pure theoretical approach, as was found by van Bladel *et al.*[12] in their study of $(NH_3)_2$.

V. THEORETICAL METHODS

In Paper I, the method used for treating the coupled intermolecular four-dimensional $(HCl)_2$ dynamics is described in detail. However, for completeness the intermolecular Hamiltonian, written in a space-fixed angular momentum coupling scheme, is reproduced below

$$\hat{H}=\frac{\hbar^2\partial^2}{2\mu\partial R^2}+b_1\hat{j}_1^2+b_2\hat{j}_2^2+\frac{\hbar^2\hat{l}^2}{2\mu R^2}+V(R,\theta_1,\theta_2,\phi). \tag{23}$$

Here μ is the reduced mass of the complex, b_1 and b_2 are the rotational constants of monomers 1 and 2, $\hat{j}_1^2$ and $\hat{j}_2^2$ are the rotational angular momentum operators for monomers 1 and 2, and $\hat{l}^2$ is the orbital angular momentum operator associated with the end-over-end rotation of the complex. For all calculations described in this work, the intramolecular coordinates are adiabatically separated from the intermolecular coordinates by fixing the HCl bond lengths at their equilibrium values.

The results of fully coupled four-dimensional dynamics calculations for $(HCl)_2$, $(DCl)_2$, and (HCl)(DCl) are also presented for the Bunker *et al.*[51] *ab initio* surface in Paper I. Those results are used here in order to compare to the available experimental spectra, as well as with the semiempirical potential of Votava *et al.*[48] (potential 3). Following the methods outlined in Paper I, the Votava *et al.* potential was expanded in a spherical expansion formalism up to $\mathbf{l}_1^{\max}=\mathbf{l}_2^{\max}=8$ in order to achieve satisfactory reproduction of the site–site potential points. Since this IPS is obviously more anisotropic than the *ab initio* surface (which required an expansion only to $\mathbf{l}_1^{\max}=\mathbf{l}_2^{\max}=5$), a very large basis set was necessary to achieve satisfactory convergence ($j_{\max}=10$ $n=5$) in the four-dimensional variational method, such that only the $J=0$ levels could be calculated with available computer resources. Therefore, the $J=0\rightarrow1$ spacings were estimated from the $\langle 1/R^2\rangle$ expectation value calculated from the eigenvectors of the $J=0$ computation. Some relevant energy level differences from this calculation are contained in Table III for comparison with the *ab initio* and experimental results for $(HCl)_2$. The Votava *et al.* potential, adjusted to fit liquid HCl data and gas phase second virial coefficients, reproduces the experimental dissociation energy and the average intermolecular distance (from the $J=0\rightarrow1$ spacings) in quite good agreement with experiment. However, it quite badly predicts the positions of the excited states in the tunneling coordinate ($\nu_5=1$ and 2), while the *ab initio* potential provides much more quantitative estimates of these features. The performance of the semiempirical potential—a relatively good description of the radial coordinate but a very poor description of the anisotropy—is not surprising, given the data set used to determine its parameters. Although the *ab initio* potential provides reasonably *qualitative* agreement with experiment, we turn to the description of a *quantitative* nonlinear least-squares approach to the determination of an improved experimental intermolecular IPS for $(HCl)_2$ exclusively from high resolution spectroscopic data.

TABLE III. Comparison of calculations using the *ab initio* (Ref. 51) and Votava *et al.* (Ref. 48) potentials to experimental results for selected eigenstates (energies in cm^{-1}) for $(HCl)_2$.

	Ab initio	Votava *et al.*	Experiment
D_0	−373	−396	−412
Ground state $J=0\rightarrow1$	0.1213	0.1295	0.1297
$\|0\ 0\ 1\ 0\rangle$	12.4	1.3	15.5
$\|0\ 0\ 1\ 0\rangle$ $J=0\rightarrow1$	0.1210	0.1295	0.1278
$\|0\ 0\ 2\ 0\rangle$	59.1	88.4	53.1
$\|0\ 0\ 2\ 0\rangle$ $J=0\rightarrow1$	0.1206	0.1275	0.1284
$\|0\ 0\ 0\ 1\rangle$	136.1	169.2	160.8
$\|0\ 0\ 0\ 1\rangle$ $J=0\rightarrow1$	0.1187	0.1267	0.1268

VI. EXPERIMENTAL DATA SET

The spectroscopic observables which are available as constraints on the nature of the $(HCl)_2$ intermolecular potential energy surface include: the dissociation energy, the intermolecular vibrational energies, the near prolate top rotational term values $[(B+C)/2$, $(B-C)$, and $A]$ and the nuclear quadrupole coupling constants ($\langle P_2(\cos\theta)\rangle$). Through a combination of high resolution laser and FTIR far-infrared and laser-based near-infrared spectroscopy experiments, many of the low-lying eigenstates of $(HCl)_2$ (Refs. 31, 33–38, 61, and 62) and $(DCl)_2$ (Refs. 34, 38, and 62) have been accessed. In the least-squares fits, we include information which is available from the $J=0$ and $J=1$ eigenvalues and the angular expectation values. The experimental data set used in the least-squares fit is summarized in Table IV for $(HCl)_2$ and in Table V for $(DCl)_2$. The eigenstates are labeled by their vibrational state $-|\nu_3\nu_4\nu_5\nu_6\rangle$—and the relevant rotational quantum numbers, J and K_a.

The extent to which the experimental data constrain the IPS is a crucial consideration in the fitting of the spectroscopic data. The new $(HCl)_2$ and $(DCl)_2$ far-infrared spectra (involving $\nu_5=2$) reported here greatly add to the characterization of the tunneling coordinate (i.e., the dependence of the potential on the in-plane bending angles). Direct far-infrared measurements of the $\nu_5=0\rightarrow1$ transition frequency[35] (including K_a dependencies)[33,36] for $(HCl)_2$ and estimates for

TABLE IV. Comparison of calculations using the *ab initio* (Ref. 51) and the fitted ES1 potentials with experimentally determined values for $(H^{35}Cl)_2$.

Observable	*Ab initio*	Experimental	ES1
$\|0\ 0\ 0\ 0\rangle$			
D_0	−373.0	−412.0	−411.8
$J=0\rightarrow1\ K_a=0\rightarrow0$	0.121 3	0.129 7	0.129 6
$J=1\rightarrow1\ K_a=1^-\rightarrow1^+$	0.000 570	0.000 624	0.000 638
$J=0\rightarrow1\ K_a=0\rightarrow1^-$	11.076 92	11.085 64	11.085 50
$\langle P_2(\cos\theta)\rangle$	0.145 0	0.170 2	0.160 1
$\|0\ 0\ 1\ 0\rangle$			
Ground state $J=0\rightarrow\nu_5=1\ J=0$	12.432 81	15.476 68	15.667 07
$J=0\rightarrow1\ K_a=0\rightarrow0$	0.121 0	0.127 8	0.127 8
$J=1\rightarrow1\ K_a=1^-\rightarrow1^+$	0.000 450	0.000 503	0.000 510
$J=0\rightarrow1\ K_a=0\rightarrow1^-$	11.101 55	10.883 49	11.062 66
$\langle P_2(\cos\theta)\rangle$	0.187 9	0.186 8	0.196 3
$\|0\ 0\ 2\ 0\rangle$			
$\nu_5=1\ J=0\rightarrow\nu_5=2\ J=0$	46.660 43	37.645 40	37.616 12
$J=0\rightarrow1\ K_a=0\rightarrow0$	0.120 6	0.128 4	0.128 6
$\langle P_2(\cos\theta)\rangle$	0.180 6	0.178 8	0.195 5
$\|0\ 0\ 0\ 1\rangle$			
Ground state $J=0\rightarrow\nu_6=1\ J=0$	136.055 73	160.778	160.601 52
$J=0\rightarrow1\ K_a=0\rightarrow0$	0.118 3	0.128 6	0.127 7
$J=1\rightarrow1\ K_a=1^-\rightarrow1^+$	0.000 520	0.000 615	0.000 583
$J=0\rightarrow1\ K_a=0\rightarrow1^-$	11.515 20	11.198	10.925 70
$\|0\ 0\ 1\ 1\rangle$			
Ground state $J=0\rightarrow\nu_6=1\ \nu_5=1\ J=0$	157.061 64	184.862	185.059 77
$J=0\rightarrow1\ K_a=0\rightarrow0$	0.118 7	0.126 8	0.125 7
$J=1\rightarrow1\ K_a=1^-\rightarrow1^+$	0.000 290	0.000 438	0.003 55
$J=0\rightarrow1\ K_a=0\rightarrow1^-$	11.149 30	8.381	8.661 30

$(DCl)_2$ from near-infrared spectroscopy[34,38] constitute the previously reported data set for this coordinate. The $\nu_5=2$ spectra are particularly important as these eigenstates are located near the top of the barrier to donor–acceptor interchange. The antigeared in-plane bending fundamental (ν_3) has yet to be observed, probably due to its small predicted band intensity. In spite of this, the dependence of the potential on the in-plane coordinates is probably constrained better by experiment than any other region of the potential. The FTIR far-infrared measurement of the out-of-plane bend for $(HCl)_2$ (Ref. 36) provides a good constraint on the torsional coordinate (ϕ) and the measurement of a similar combination out-of-plane bend/$\nu_5=1$ band provides a constraint on the extent of the coupling of ϕ to the in-plane angles (θ_1 and θ_2). Unfortunately, no spectra accessing excited stretching states have been reported; such data would provide the most exacting constraint on the radial coordinate. However, the $J=0\rightarrow1$ spacings are largely determined by $\langle 1/R^2\rangle$ and therefore provide a good constraint on the average value of R for each bending state. In addition, the dissociation energy (D_0) for $(HCl)_2$ has been measured from a consideration of absolute infrared intensities,[61] and this information helps to constrain the isotropically averaged well depth. In order to compare the experimental dissociation energy directly with the results from the intermolecular four-dimensional dynamics calculations, it is necessary to properly account for the change in zero-point energy upon complexation due to shifts in the *intramolecular* frequencies. The ν_1 "free" and ν_2 "bonded" HCl stretches have been measured at 2880.2495 and 2854.0593 cm^{-1}, respectively.[37] Since the HCl monomer stretching frequency occurs at 2885.9777 cm^{-1}, this amounts to a total redshift of 38 cm^{-1}, or a decrease in the zero-point energy of 19 cm^{-1}. Therefore, the experimentally determined D_0 of 431 cm^{-1} is shifted to 412 cm^{-1} so as to include contributions from the intermolecular modes only. It should also be emphasized that the $(DCl)_2$ spectra essentially con-

TABLE V. Comparison of calculations using the *ab initio* (Ref. 51) and the fitted ES1 potentials with experimentally determined values for $(D^{35}Cl)_2$.

Observable	*Ab initio*	Experimental	ES1
$\|0\ 0\ 0\ 0\rangle$			
$J=0\rightarrow1\ K_a=0\rightarrow0$	0.120 4	0.128 1	0.128 1
$J=1\rightarrow1\ K_a=1^-\rightarrow1^+$	0.000 942	0.001 2	0.001 06
$\|0\ 0\ 1\ 0\rangle$			
Ground state $J=0\rightarrow\nu_5=1\ J=0$	3.633 62	5.96	5.734 94
$J=0\rightarrow1\ K_a=0\rightarrow0$	0.120 1	0.126 5	0.126 8
$J=1\rightarrow1\ K_a=1^-\rightarrow1^+$	0.000 828	0.000 926	0.000 906
$J=0\rightarrow1\ K_a=0\rightarrow1^-$	5.608 63	5.512 18	5.539 59
$\langle P_2(\cos\theta)\rangle$	0.193 1	0.188 7	0.193 1
$\|0\ 0\ 2\ 0\rangle$			
$\nu_5=1\ J=0\rightarrow\nu_5=2\ J=0$	35.858 79	31.012 25	30.984 97
$K=0\rightarrow1\ K_a=0\rightarrow0$	0.120 5	0.128 9	0.128 9
$J=1\rightarrow1\ K_a=1^-\rightarrow1^+$	0.001 06	0.001 20	0.001 18
$J=0\rightarrow1\ K_a=0\rightarrow1^-$	5.223 48	5.419 45	5.275 01
$\langle P_2(\cos\theta)\rangle$	0.165 5	0.192 8	0.186 1

stitute an independent data set due to the fact that DCl possesses a much smaller rotational constant than HCl. This results in the $(DCl)_2$ eigenstates being localized in quite different regions of the potential surface than the corresponding $(HCl)_2$ eigenstates.

VII. LEAST-SQUARES FITS

The fully coupled four-dimensional dynamics calculation was imbedded in a standard nonlinear least-squares fitting routine (Levenberg–Marquardt algorithm)[63] using a basis set of $j_{max}=8$ $n=4$ for both $(HCl)_2$ and $(DCl)_2$. The largest matrices (for $J=1$ B^- symmetry) were 1620 basis functions square. In order to expedite the fit, only $(DCl)_2$ potential basis functions with coefficients larger than 0.1 cm^{-1} were included in the energy calculation. The effects of this approximation were found to be less than the inaccuracies due to the lack of total basis set convergence. Basis set convergence was investigated for the final fitted potential, but since the results closely paralleled the findings reported in Paper I for the *ab initio* potential, we do not explicitly report these properties. One-sided numerical derivatives were used in the least-squares procedure such that each iteration required $n_{\text{parameters}}+1$ calls to the energy subroutine. The radial basis set was precontracted using the $V_{\text{eff}}^{\text{cut}}(R)$ potential method at each least-squares iteration (also described in Paper I). This was an important consideration—especially for the initial fits—since the potential could shift substantially between iterations. Because some energy levels crossed during the course of the fitting process [in particular for $(HCl)_2$, $|0\ 0\ 2\ 0\rangle$ and $|0\ 1\ 0\ 0\rangle$], a simple eigenvalue number assignment was not sufficient to identify the desired energy differences. To distinguish between the bending and stretching states, the eigenvectors were used to sum up the total excited state radial contribution to the wave function, thus allowing identification of the stretching states. In a typical fit of eight parameters requiring five iterations for least-squares convergence, about 50 calls to the energy subroutine are necessary. The total CPU time (on our IBM RISC 6000 model 560 computer) required for a typical fit was usually about 50 h. Based mainly on the basis set convergence properties and in some cases on experimental uncertainties, the following uncertainties were assigned to each type of experimental data: (1) vibrational band origins—0.3 cm^{-1}, (2) $J=0\rightarrow1$ $K_a=0\rightarrow0$ spacings—0.0002 cm^{-1}, (3) $J=0\rightarrow1$ $K_a=0\rightarrow1$—spacings—0.1 cm^{-1}, (4) $J=1\rightarrow1$ $K_a=1^-\rightarrow1^+$ spacings—0.0001 cm^{-1}, and (5) angular expectation values $(\langle P_2(\cos\theta)\rangle)-0.01$. The uncertainty for the dissociation energy was set at the experimental estimate[61] of 22 cm^{-1} and the rotational term value uncertainties for the $|0\ 0\ 0\ 1\rangle$ and $|0\ 0\ 1\ 1\rangle$ states were doubled due to slower basis set convergence for these levels.

In their analytical fit of the *ab initio* potential, Bunker *et al.*[51] used 27 variable intermolecular parameters. Given the current experimental data set, it is not practical to attempt to vary all 27 of these parameters in a least-squares fit. Initially, we intended to use a simpler model for the potential energy surface by fixing the electrostatic, induction, and dispersion forces according to their known asymptotic long-range form and basically determining the sum of the repulsive terms and errors in the long-range terms by direct fitting to the experimental data. This approach has been successfully applied to the ArHF,[9] ArHCl,[8] ArH_2O,[10] and $ArNH_3$ (Ref. 11) systems. However, despite the fact that the electrostatic forces are indeed the source of most of the anisotropy at the radial potential minimum, trial potentials containing estimates (from SCF *ab initio* calculations)[46] for the anisotropic repulsive terms did not lead to a convergent least-squares fitting result. Because of the limited data set and the complexity of the IPS, it is crucial to possess a reasonably accurate initial potential which can then be iteratively refined by nonlinear least-squares regression. In particular, the repulsive anisotropy simply cannot be determined completely by the available data and must be adequately constrained by other (theoretical) means. The apparent difficulty in obtaining a good initial potential is the splicing of the short- and long-range contributions together at an intermolecular distance where the two contributions nearly cancel. If the two contributions are not very closely distance consistent (i.e., the breakdown of the long-range expressions at the radial minimum), the resulting potential could be substantially in error. Despite many trials, no potentials with a fixed long-range form and variable short-range terms led to convergent fitting results.

Of course, the *ab initio* potential is not plagued by the above problems which occur when the potential is partitioned into short- and long-range terms, as is common in the theory of intermolecular forces. On the other hand, it is difficult to perform *ab initio* calculations at high enough levels of theory to reproduce the correct long-range behavior, particularly for systems wherein dispersion is the dominant force. In their fitting of the analytical potential model to the *ab initio* points, Bunker *et al.* fixed the dipole, quadrupole, and octupole moments at their *ab initio* values so the analytical function would approximately retain the correct long-range electrostatic behavior.[51] The *ab initio* values for the dipole and quadrupole moments are in very good agreement with experiment, such that this constraint ensures an ''experimentally'' accurate long-range electrostatic form. However, Bunker *et al.* did not explicitly include induction terms, nor did they assess the quantitative accuracy of the terms attributed to dispersion. In order to explore the total long-range validity of the *ab initio* potential, we used the canonical long-range expressions[64] to estimate the electrostatic (from the *ab initio* dipole, quadrupole, and octupole moments), induction (from the *ab initio* moments and the experimental polarizabilities),[65] and dispersion (from estimates for the C_6 coefficient)[66] contributions at the potential minimum. The partitioning of the long-range attractive forces was as follows: the electrostatic forces (of which 93% arise from the dipole–quadrupole and quadrupole–quadrupole interactions) accounted for 470 cm^{-1}, the induction forces accounted for only 40 cm^{-1}, and the dispersion forces contributed 250 cm^{-1}. Since this estimate predicts the dispersion forces to be dominated by the electrostatic forces at the minimum, the *ab initio* potential should provide a reasonable—but not quantitative—model at both short- and long-range. Although the induction effects are perhaps safely neglected in light of the uncertainty in the larger and similarly aniso-

tropic electrostatic terms, it should be pointed out that the terms in the *ab initio* potential which correlate to dispersion predict a substantially larger contribution to the total energy than are expected from a consideration of the long-range dispersion expansion. Therefore, we simply sought to refine the parameters from the analytical *ab initio* potential to fit the spectroscopic data.

As stated earlier, it is not practical to fit all 27 intermolecular parameters in the analytical *ab initio* potential to only 33 spectroscopic observables. Our initial approach was to fit only the low-order terms and exponential reference distance that are associated with the repulsive forces. However, closer examination of the *ab initio* surface revealed that the higher order electrostatic terms (determined empirically from the fitting process and not necessarily related to the true electrostatic moments) greatly influenced the nature of the tunneling pathway. Eventually, all moments up to the 32-pole—except for the dipole moment—were allowed to vary in the fit, although the quadrupole moment actually changed very little from its initialized value. Because the *ab initio* terms that closely correlate to the long-range dispersion forces (k_6^{000}, k_6^{022}, and k_7^{011}) were approximately twice as large as expected from the long-range expressions, the k_6^{000} coefficient was fixed at roughly half the *ab initio* value in order to force a somewhat more realistic long-range character to the fitted potential. Because of the observed high correlation with the k_1^{000} parameter, the k_6^{000} term could not be directly determined in the fit. Based on the results of preliminary fits, the k_1^{022} was also fixed at a value other than that determined in the *ab initio* analytical fit. Other than the k_6^{000} and k_1^{022} terms, however, all other parameters were either held fixed to the *ab initio* values or directly varied in the least-squares fits.

The values of the parameters in the fitted potential are presented in Table VI, and the correlation matrix for the fitted terms is presented in Table VII. The dimensionless standard error (DSE)[63] was determined to be 1.14 (a value of one indicates the residuals from the fit are in perfect accordance with estimated uncertainties). The values for the 33 spectroscopic observables calculated from the fitted potential surface are contained in Tables IV and V for comparison with experimental and *ab initio* results.

TABLE VI. Values of nonzero parameters in the *ab initio* (Ref. 51) and ES1 potential energy surfaces (atomic units).

Parameter	*Ab initio* value	ES1 value[a]
a	3.07	b
b	186	b
c_1	2.412 008	b
c_2	7.35	7.468(17)
c_3	1.0	b
k_1^{sr}	0.017 0	0.017 0 (fixed)
k_2^{sr}	0.009 79	0.009 79 (fixed)
k_0^{000}	−41 008.832 48	b
k_1^{000}	0.077 5	0.022 7(40)
k_2^{000}	0.021 36	0.021 36 (fixed)
k_6^{000}	−16 964	−10 000 (fixed)
k_{11}^{000}	7.418 3	b
$k_1^{001}=-k_1^{101}$	−0.012 76	−0.005 3(11)
$k_3^{011}=-k_3^{101}$	−0.000 498	−0.000 498 (fixed)
$k_7^{011}=-k_7^{101}$	11 218	11 218 (fixed)
$k_9^{011}=-k_{10}^{101}$	−0.013 2	b
$k_1^{022}=k_1^{202}$	0.003 72	−0.002 21 (fixed)
$k_6^{022}=k_6^{202}$	−543	−543 (fixed)
$k_3^{033}=-k_3^{303}$	−0.000 3646	−0.000 488(34)
$k_9^{033}=-k_9^{303}$	0.007 98	b
$k_4^{044}=k_4^{404}$	0.000 0300	0.000 0300 (fixed)
$k_7^{055}=-k_7^{505}$	191	191 (fixed)
k_4^{110}	−0.000 0499	−0.000 0499 (fixed)
$k_{10}^{121}=-k_9^{211}$	0.005 06	b
$k_1^{123}=-k_1^{213}$	−0.000 241	−0.000 241 (fixed)
$k_9^{123}=-k_{10}^{213}$	0.002 55	b
k_5^{222}	0.000 0084	0.000 0084 (fixed)
k_9^{224}	0.004 57	b
$k_9^{231}=-k_{10}^{321}$	0.004 00	b
$k_9^{233}=-k_{10}^{323}$	0.008 81	b
$k_7^{235}=-k_7^{325}$	286	286 (fixed)
$k_{10}^{235}=-k_9^{325}$	−0.003 66	b
$k_1^{242}=k_1^{422}$	0.000 137	0.000 137 (fixed)
$k_1^{244}=k_1^{424}$	0.000 122	0.000 122 (fixed)
$k_7^{246}=k_7^{426}$	343	343 (fixed)
$k_{10}^{246}=k_9^{426}$	0.001 53	b
$k_7^{257}=-k_7^{527}$	−243	−243 (fixed)
k_8^{336}	1459	1459 (fixed)
Q_1	0.427 71	0.427 71 (fixed)
Q_2	2.776 35	2.594(23)
Q_3	3.748 7	2.86(37)
Q_4	8.527	1.79(35)
Q_5	16.96	21.4(3.7)

[a]Number in parentheses: one standard deviation uncertainty.
[b]Intramolecular parameters.

TABLE VII. Correlation matrix.

	c_2	k_1^{000}	k_1^{011}	k_3^{033}	Q_2	Q_3	Q_4	Q_5
c_2	1.00							
k_1^{000}	−0.75	1.00						
k_1^{011}	0.02	0.64	1.00					
k_3^{033}	0.53	−0.01	0.58	1.00				
Q_2	−0.31	0.15	−0.22	−0.33	1.00			
Q_3	0.19	−0.77	−0.93	−0.45	−0.11	1.00		
Q_4	0.06	0.25	0.44	0.32	−0.17	−0.38	1.00	
Q_5	0.31	−0.64	−0.55	−0.46	−0.45	0.75	−0.14	1.00

VIII. RELIABILITY OF THE FITTED INTERMOLECULAR POTENTIAL ENERGY SURFACE

The DSE of the fit indicates that the spectroscopic observables were approximately fit within their estimated uncertainties, indicating that the fitted potential (which we hereafter refer to as ES1) satisfactorily reproduces the large set of high precision spectroscopic observables. In addition, the correlations between the fitted parameters are quite low, with only one pair of parameters correlated at a level above 0.77. Although it is not possible to assess the uniqueness of the ES1 potential, the fit satisfies the basic requirements of precisely reproducing all available observables with an independent set of parameters. Of course, since the ES1 surface was forced to reproduce results from spectroscopy experiments alone, it may be reliable only in the bound region of the potential. However, because the short-range terms were held fixed at their *ab initio* values and an effort was made to ensure a valid long-range form, it is hoped that the ES1 potential may be reasonably reliable in regions that were not probed directly by spectroscopy. A similarly determined po-

tential for $ArNH_3$ has recently been shown to accurately reproduce the results of state-selected scattering experiments which probe much higher energy regions of the potential than were accessed by the spectroscopy experiments.[67] Because of the lack of experimental information on the excited van der Waals stretching states, the primary weakness in the ES1 potential is probably in the radial degree of freedom. It should be noted, however, that the fitted potential produces the $J=0\rightarrow1$ energy differences (proportional to $\langle 1/R^2\rangle$) for all states that are in much better agreement with experiment than does the *ab initio* potential. These observables also serve to constrain the degree of angular–radial coupling, an important point which will discussed in a later section. The in-plane coordinates, although extensively characterized near the minimum and the donor–acceptor interchange barrier, are only constrained by experiment at relatively low energies, as discussed earlier. Measurements of both the ν_3 antigeared in-plane bending fundamental and the ν_4 intermolecular stretching fundamental will be necessary to extend the reliability of the ES1 surface to higher energies for these coordinates.

As a further test of the reliability of the ES1 potential surface (with respect to the radial coordinate, in particular), the temperature dependence of the second virial coefficients were calculated and compared to the experimental results[49] as well as with the results calculated from the *ab initio* potential (the Votava *et al.* potential was already adjusted to fit these coefficients). In order to calculate second virial coefficients for $(HCl)_2$, the following integral must be evaluated:

$$B(T)=\frac{N_{\mathrm{av}}}{4}\int_0^{2\pi}\int_0^{\pi}\int_0^{\pi}\int_0^{\infty}(1-\exp[-V(R,\theta_1,\theta_2,\phi)/kT])\times\sin\,\theta_1\,\sin\,\theta_2\;R^2 d\phi d\theta_1 d\theta_2 dR, \tag{24}$$

where N_{Av} is Avogadro's number and $B(T)$ is expressed in cm^3/mol. At very short range, the exponential term is zero and the integral can be evaluated analytically. For $(HCl)_2$, the integral is evaluated analytically for $R=0$–2 Å and numerically evaluated (by Simpson's rule) for 2 Å $<R<$30 Å. Because no Gaussian quadratures are applicable to this integral, the numerical evaluation requires 100 points in R and 6 points in each angular coordinate (to achieve accuracies of $\sim$10 cm^3/mol) and is therefore too expensive to include in the least-squares fitting process. In Fig. 3 we present a comparison of the experimental and calculated second virial coefficients. It is clear that the ES1 potential satisfactorily reproduces the experimental second virial coefficients while the *ab initio* potential does not. These results seem to indicate that the radial dependence of the ES1 potential is at least as accurate as the Votava *et al.* potential for the regions of the potential probed by the second virial coefficients. The ES1 potential is, of course, much more accurate than the Votava *et al.* potential in the bound region of the potential, particularly with respect to the angular coordinates.

Additional spectroscopic measurements will provide a precise test of the accuracy of the new potential described here, and will permit further details of the intermolecular forces in this system to be elucidated. To aid in this endeavor, the ES1 potential was used to calculate energy levels

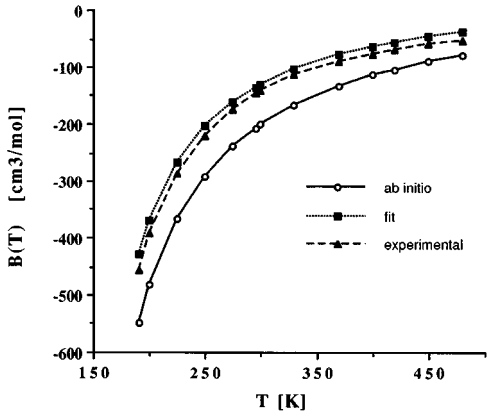

FIG. 3. Calculated and experimental second virial coefficients for HCl.

for $(HCl)_2$ and $(DCl)_2$ using a $j_{\max}=8$ and $n=4$ basis and the results are presented in Table VIII. In addition, calculations for (HCl)(DCl) were also performed (in a manner identical to calculations using the *ab initio* potential) using the ES1 surface and are presented in Table IX. We find that the (HCl)(DCl) isomer with the DCl monomer acting as the hydrogen bond donor is 22 cm^{-1} more stable than the corresponding isomer with HCl subunit as the donor, which is in good agreement with the recent experimental estimate of 16 ± 4 cm^{-1} obtained by a consideration of near-infrared band intensities.[68] Although the energy levels are reported to many digits, the reader should refer to the basis set convergence section in Paper I for an estimate of the actual number of significant figures. There are many VRT states of interest that have not yet been measured. In Table X we list several frequencies and intensities for transitions which access states that would be of particular utility in a testing of the new ES1 potential. The intensities were calculated according to the method outlined in the accompanying paper; however, the Boltzmann factors were left out so that the intensities could be easily weighted either for the 5 K molecular beam or the 140 K cooled cell experiments.

Intensities for transitions already measured are presented for comparison. For example, the $(HCl)_2$ $|0\ 0\ 0\ 0\rangle$ $J=0$ $K_a=0\rightarrow|0\ 0\ 1\ 0\rangle$ $J=1$ $K_a=0$ transition (to which the other transitions are normalized) was measured using the tunable far-infrared laser technique with a signal-to-noise ratio in excess of 1000:1.[35] The ν_6 out-of-plane bending fundamental has not yet been reported for $(DCl)_2$, although such work is in progress.[69] The measurement of this state (in addition to the combination state $|0\ 0\ 1\ 1\rangle$) would provide an indication of the reliability of the out-of-plane dependence of the ES1 potential. Of course, measurements of excited van der Waals stretching states would provide important information on the radial dependence of the potential. Intensities calculated using the *ab initio* potential predicted that transitions involving the van der Waals stretching states would be too weak to observe with current experimental techniques. However, the results from the ES1 potential indicate that the $(HCl)_2$ $|0\ 0\ 1\ 0\rangle$ $J=0$ $K_a=0\rightarrow|0\ 1\ 0\ 0\rangle$ $J=1$ $K_a=0$ or 1 transitions may indeed be detectable, although the Boltzmann factor for the 5 K molecular beam experiment is quite unfavorable. The

TABLE VIII. Calculated energy levels from the ES1 potential surface (in cm^{-1}).

Assignment	$(H^{35}Cl)_2$		$(D^{35}Cl)_2$	
	$J=0$	$J=1$	$J=0$	$J=1$
	A^+ symmetry	B^- symmetry	A^+ symmetry	B^- symmetry
$\|0\ 0\ 0\ 0\rangle K_a=0$	−411.783 68	−411.654 04	−469.412 94	−469.284 76
$\|0\ 0\ 0\ 0\rangle K_a=1^-$		−400.698 19		−463.852 90
$\|0\ 1\ 0\ 0\rangle K_a=0$	−339.716 63	−339.591 86	−398.672 77	−398.549 71
$\|0\ 0\ 2\ 0\rangle K_a=0$	−358.500 52	−358.371 93	−432.673 40	−432.544 44
$\|0\ 1\ 0\ 0\rangle K_a=1^-$		−328.907 39		−393.268 73
$\|0\ 0\ 2\ 0\rangle K_a=1^-$		−347.278 03		−427.399 68
$\|0\ 2\ 0\ 0\rangle K_a=0$	−275.897 62	−275.774 89	−335.428 55	−335.309 78
$\|0\ 2\ 0\ 0\rangle K_a=1^-$		−265.005 79		−330.094 67
$\|0\ 1\ 2\ 0\rangle K_a=0$	−300.612 89	−300.487 89	−359.444 98	−359.321 02
$\|0\ 1\ 2\ 0\rangle K_a=1^-$		−288.994 89		−353.787 16
$\|0\ 0\ 4\ 0\rangle K_a=0$	−264.037 45	−263.910 83	−379.403 41	−379.277 02
$\|0\ 0\ 4\ 0\rangle K_a=1^-$		−250.046 50		−373.402 99
$\|0\ 2\ 2\ 0\rangle K_a=0$	−234.530 10	−234.402 43	−301.174 21	−301.050 41
$\|0\ 2\ 2\ 0\rangle K_a=1^-$		−222.680 02		−296.076 62
$\|0\ 0\ 1\ 1\rangle K_a=1^+$		−218.060 84		−330.898 46
$\|0\ 1\ 4\ 0\rangle K_a=0$	−203.356 09	−203.233 64	−322.996 96	−322.874 11
$\|0\ 1\ 4\ 0\rangle K_a=1^-$		−188.399 15		−317.048 13
$\|0\ 0\ 6\ 0\rangle K_a=0$	−184.741 73	−184.614 27	−289.892 14	−289.770 31
$\|1\ 0\ 0\ 0\rangle K_a=0$	−171.032 60	−170.909 30	−283.079 61	−282.954 91
$\|0\ 0\ 6\ 0\rangle K_a=1^+$		−168.016 87		−284.377 18
$\|0\ 1\ 1\ 1\rangle K_a=1^+$		−163.790 72		−278.863 81
$\|1\ 0\ 0\ 0\rangle K_a=1^-$		−155.362 52		−275.765 75
	A^- symmetry	B^+ symmetry	A^- symmetry	B^+ symmetry
$\|0\ 0\ 1\ 0\rangle K_a=1^+$		−385.053 29		−458.076 54
$\|0\ 1\ 1\ 0\rangle K_a=1^+$		−320.948 64		−384.042 08
$\|0\ 0\ 3\ 0\rangle K_a=1^+$		−295.914 87		−402.787 65
$\|0\ 2\ 1\ 0\rangle K_a=1^+$		−258.721 93		−326.694 85
$\|0\ 0\ 0\ 1\rangle K_a=0$	−251.182 21	−251.054 50	−347.155 05	−347.027 49
$\|0\ 0\ 0\ 1\rangle K_a=1^-$		−240.256 83		−341.352 98
$\|0\ 1\ 3\ 0\rangle K_a=1^+$		−231.814 40		−345.201 55
$\|0\ 1\ 0\ 1\rangle K_a=0$	−199.862 07	−199.737 52	−308.891 40	−308.764 45
$\|0\ 1\ 0\ 1\rangle K_a=1^-$		−189.873 83		−277.833 79
$\|0\ 0\ 5\ 0\rangle K_a=1^-$		−207.017 16		−316.087 89
$\|0\ 2\ 3\ 0\rangle K_a=1^+$		−176.274 64		−286.558 99
$\|0\ 0\ 2\ 1\rangle K_a=0$	−179.911 07	−179.786 19	−283.180 37	−283.058 37
	B^+ symmetry	A^- symmetry	B^+ symmetry	A^- symmetry
$\|0\ 0\ 1\ 0\rangle K_a=0$	−396.116 46	−395.988 61	−463.615 86	−463.489 02
$\|0\ 0\ 1\ 0\rangle K_a=1^-$		−385.053 80		−458.077 44
$\|0\ 1\ 1\ 0\rangle K_a=0$	−332.254 25	−332.130 81	−389.374 30	−389.251 87
$\|0\ 1\ 1\ 0\rangle K_a=1^-$		−320.949 14		−384.042 93
$\|0\ 0\ 3\ 0\rangle K_a=0$	−307.861 79	−307.735 01	−408.332 41	−408.206 08
$\|0\ 0\ 3\ 0\rangle K_a=1^-$		−295.915 39		−402.788 60
$\|0\ 2\ 1\ 0\rangle K_a=0$	−270.248 17	−270.123 70	−332.498 11	−332.375 63
$\|0\ 2\ 1\ 0\rangle K_a=1^-$		−258.722 46		−326.695 63
$\|0\ 1\ 3\ 0\rangle K_a=0$	−244.289 88	−244.167 45	−350.878 28	−350.754 87
$\|0\ 0\ 0\ 1\rangle K_a=1^+$		−240.256 24		−341.351 95
$\|0\ 1\ 3\ 0\rangle K_a=1^-$		−231.814 84		−345.202 38
$\|0\ 0\ 5\ 0\rangle K_a=0$	−223.791 56	−223.664 39	−321.414 63	−321.294 51
$\|0\ 2\ 3\ 0\rangle K_a=0$	−190.476 89	−190.350 69	−292.893 96	−292.771 34
$\|0\ 1\ 0\ 1\rangle K_a=1^+$		−189.873 10		−277.832 92
$\|0\ 0\ 5\ 0\rangle K_a=1^-$		−207.017 07		−316.088 61
$\|0\ 2\ 3\ 0\rangle K_a=1^-$		−176.274 64		−286.559 75
	B^- symmetry	A^+ symmetry	B^- symmetry	A^+ symmetry
$\|0\ 0\ 0\ 0\rangle K_a=1^+$		−400.697 55		−463.851 84
$\|0\ 1\ 0\ 0\rangle K_a=1^+$		−328.906 78		−393.267 74
$\|0\ 0\ 2\ 0\rangle K_a=1^+$		−347.277 27		−427.398 51
$\|0\ 2\ 0\ 0\rangle K_a=1^+$		−265.005 13		−330.093 89
$\|0\ 1\ 2\ 0\rangle K_a=1^+$		−288.994 12		−353.786 26
$\|0\ 0\ 4\ 0\rangle K_a=1^+$		−250.046 17		−373.401 94
$\|0\ 0\ 1\ 1\rangle K_a=0$	−226.723 78	−226.598 09	−335.920 02	−335.794 46
$\|0\ 2\ 2\ 0\rangle K_a=1^+$		−222.679 38		−296.076 06
$\|0\ 0\ 1\ 1\rangle K_a=1^-$		−218.061 19		−330.899 27
$\|0\ 1\ 4\ 0\rangle K_a=1^+$		−188.399 06		−317.047 14
$\|0\ 1\ 1\ 1\rangle K_a=0$	−171.514 40	−171.393 00	−283.259 72	−283.135 61
$\|0\ 0\ 6\ 0\rangle K_a=1^-$		−168.017 73		
$\|0\ 1\ 1\ 1\rangle K_a=1^-$		−163.790 72		−278.864 79
$\|1\ 0\ 0\ 0\rangle K_a=1^+$		−155.361 96		

TABLE IX. Energy levels, expectation values, and relative absorption intensities ($J=0\rightarrow1$ transitions originating from ground state) for (HCl)(DCl) calculations using the ES1 potential.

State	K_a	E (cm^{-1})	$\langle P_1\rangle_1$[a]	$\langle P_2\rangle_1$	$\langle P_1\rangle_2$	$\langle P_2\rangle_2$	$I_{i\leftarrow1}$[b]
1	0	−427.2	0.023	−0.336	−0.905	0.752	0.0003
	1	−416.5					1.0000
2	0	−405.0	0.838	0.649	−0.101	−0.314	0.1276
	1	−398.9					0.1523
3	0	−372.7	0.379	0.110	−0.555	0.284	0.3207
	1	−365.3					0.3334
4	0	−343.1	0.454	0.309	−0.337	0.166	0.0773
	1	−336.1					0.0120
5	0	−307.2	0.379	0.296	−0.320	0.245	0.0017
	1	−300.6					0.0026
6	0	−303.6	0.013	−0.334	−0.852	0.610	0.0000
	1	−289.6					0.2921

[a]$\langle P_j\rangle_i$ signifies the expectation value of the jth Legendre polynomial for the ith subunit: 1=HCl, 2=DCl.
[b]Transition intensities normalized to largest value.

$(DCl)_2$ $|0\ 0\ 0\ 0\rangle$ $J=0$ $K_a=0\rightarrow|0\ 1\ 1\ 0\rangle$ $J=1$ $K_a=0$ or 1 transitions appear to be better candidates for molecular beam experiments since they originate from the ground state. The dramatic differences in the transition intensities for these excited van der Waals stretching states is another manifestation of the important effects of angular–radial coupling. Measurements of the ν_3 antigeared in-plane bending fundamental and the $|0\ 0\ 3\ 0\rangle$ geared in-plane bending overtone for both $(HCl)_2$ and $(DCl)_2$ would provide additional information on the in-plane dependence of the potential. Frequencies and intensities for transitions involving these states are also contained in Table X. If some or all of these states could be measured, it is likely that further improvements in the IPS could be obtained.

IX. COMPARISON AND EVALUATION OF THE $(HCl)_2$ INTERMOLECULAR POTENTIAL ENERGY SURFACES

In Table XI, the available high quality $(HCl)_2$ potential surfaces, including the ES1 surface, are described by specifying their global minima and C_{2h} barrier energies and geometries. The ES1 potential, with a global energy minimum of 692 cm^{-1} at $R=3.746$ Å, $\theta_1=9°$, $\theta_2=89.8°$, and $\phi=180°$, is qualitatively similar to the *ab initio* potentials[44,50,51] presented in Table XI and to the Votava *et al.*[48] surface. The *ab initio* IPS of Karpfen *et al.*[37] is actually very complicated, exhibiting four different saddle points below the dimer dissociation energy. However, the lowest C_{2h} saddle is fairly well separated from the others (by at least 340 cm^{-1}) and is expected to dominate the *trans* donor–acceptor tunneling dynamics. The donor–acceptor interchange tunneling pathway in the ES1 surface is of particular interest here. In Fig. 4, a contour plot (with R and ϕ fixed at their potential minimum values) is presented showing the in-plane dependence and the donor–acceptor interchange tunneling pathway of the ES1 potential surface. Corresponding plots for the *ab initio* and the Votava *et al.* potentials would appear similar except for the difference in barrier heights. It is found that the ES1 and *ab initio* potentials possess similar tunneling barriers (ranging from 45 to 71 cm^{-1}), while the Votava potential has a much higher barrier (188 cm^{-1} in the single center spherical expanded form) to donor–acceptor interchange. However, the θ_1 vs θ_2 at fixed R contour plots do not reveal all of the important details of the tunneling pathway (including the actual minimum energy pathway). In Figs. 5–7, contour plots of R vs θ_1, with θ_2 and ϕ determined by an energy minimization algorithm, are presented for all three potentials. These graphs are more revealing than the θ_1 vs θ_2 plots, since θ_2 has a nearly linear dependence on θ_1 for the coordinate range of interest. The R vs θ_1 contour plots clearly show that the *ab initio* tunneling pathway does not posses a significant radial dependence while the ES1 potential shows a clear preference for a decrease in the center of mass separation at the C_{2h} barrier geometry. In addition, it should be noted that the *ab initio* and ES1 potentials are plotted on the same scale in order to emphasize the shorter average intermolecular separation and the stiffer radial dependence of the ES1 potential.

Although the ES1 barrier is only 16 cm^{-1} lower than the

TABLE X. Selected predicted transition frequencies and relative intensities from ES1 potential.

Initial state	Final state	ν (cm^{-1})	Intensity
$(HCl)_2$			
$\|0\ 0\ 0\ 0\rangle J=0$ $K_a=0$	$\|0\ 0\ 1\ 0\rangle J=1$ $K_a=0$	15.795 07	1.000 00
$\|0\ 0\ 1\ 0\rangle J=0$ $K_a=0$	$\|0\ 0\ 2\ 0\rangle J=1$ $K_a=0$	37.744 53	1.167 67[a]
$\|0\ 0\ 0\ 0\rangle J=0$ $K_a=0$	$\|0\ 0\ 0\ 1\rangle J=1$ $K_a=1$	171.527 44	0.741 22
$\|0\ 0\ 1\ 0\rangle J=0$ $K_a=0$	$\|0\ 0\ 1\ 1\rangle J=1$ $K_a=1$	178.055 27	0.791 70[a]
$\|0\ 0\ 0\ 0\rangle J=0$ $K_a=0$	$\|0\ 1\ 1\ 0\rangle J=1$ $K_a=0$	79.523 23	0.000 11
$\|0\ 0\ 0\ 0\rangle J=0$ $K_a=0$	$\|0\ 1\ 1\ 0\rangle J=1$ $K_a=1$	90.834 54	0.001 48
$\|0\ 0\ 1\ 0\rangle J=0$ $K_a=0$	$\|0\ 1\ 0\ 0\rangle J=1$ $K_a=0$	56.524 60	0.556 84[a]
$\|0\ 0\ 1\ 0\rangle J=0$ $K_a=0$	$\|0\ 1\ 0\ 0\rangle J=1$ $K_a=1$	67.209 07	0.279 54[a]
$\|0\ 0\ 0\ 0\rangle J=0$ $K_a=0$	$\|0\ 0\ 3\ 0\rangle J=1$ $K_a=0$	104.048 67	0.039 72
$\|0\ 0\ 0\ 0\rangle J=0$ $K_a=0$	$\|0\ 0\ 3\ 0\rangle J=1$ $K_a=1$	115.868 29	0.039 47
$\|0\ 0\ 0\ 0\rangle J=0$ $K_a=0$	$\|1\ 0\ 1\ 0\rangle J=1$ $K_a=0$	252.937 47	0.089 67
$\|0\ 0\ 0\ 0\rangle J=0$ $K_a=0$	$\|1\ 0\ 1\ 0\rangle J=1$ $K_a=1$	262.704 21	0.279 95
$\|0\ 0\ 1\ 0\rangle J=0$ $K_a=0$	$\|1\ 0\ 0\ 0\rangle J=1$ $K_a=0$	225.207 16	0.112 60[a]
$\|0\ 0\ 1\ 0\rangle J=0$ $K_a=0$	$\|1\ 0\ 0\ 0\rangle J=1$ $K_a=1$	240.753 94	0.272 04[a]
$(DCl)_2$			
$\|0\ 0\ 0\ 0\rangle J=0$ $K_a=0$	$\|0\ 0\ 1\ 0\rangle J=1$ $K_a=0$	5.795 74	1.000 00
$\|0\ 0\ 1\ 0\rangle J=0$ $K_a=0$	$\|0\ 0\ 2\ 0\rangle J=1$ $K_a=0$	31.071 42	1.985 43[a]
$\|0\ 0\ 0\ 0\rangle J=0$ $K_a=0$	$\|0\ 1\ 1\ 0\rangle J=1$ $K_a=0$	80.161 07	0.130 30
$\|0\ 0\ 0\ 0\rangle J=0$ $K_a=0$	$\|0\ 1\ 1\ 0\rangle J=1$ $K_a=1$	85.370 01	0.052 45
$\|0\ 0\ 1\ 0\rangle J=0$ $K_a=0$	$\|0\ 1\ 0\ 0\rangle J=1$ $K_a=0$	65.066 15	0.165 98[a]
$\|0\ 0\ 1\ 0\rangle J=0$ $K_a=0$	$\|0\ 1\ 0\ 0\rangle J=1$ $K_a=1$	70.347 16	0.062 28[a]
$\|0\ 0\ 0\ 0\rangle J=0$ $K_a=0$	$\|0\ 0\ 3\ 0\rangle J=1$ $K_a=0$	61.206 86	0.187 35
$\|0\ 0\ 0\ 0\rangle J=0$ $K_a=0$	$\|0\ 0\ 3\ 0\rangle J=1$ $K_a=1$	66.624 34	0.022 29
$\|0\ 0\ 0\ 0\rangle J=0$ $K_a=0$	$\|0\ 0\ 0\ 1\rangle J=1$ $K_a=1$	128.060 99	0.734 15
$\|0\ 0\ 1\ 0\rangle J=0$ $K_a=0$	$\|0\ 0\ 1\ 1\rangle J=1$ $K_a=1$	132.717 40	0.948 03[a]
$\|0\ 0\ 0\ 0\rangle J=0$ $K_a=0$	$\|1\ 0\ 1\ 0\rangle J=1$ $K_a=0$	193.705 52	0.206 18
$\|0\ 0\ 0\ 0\rangle J=0$ $K_a=0$	$\|1\ 0\ 1\ 0\rangle J=1$ $K_a=1$	201.235 18	0.740 75
$\|0\ 0\ 1\ 0\rangle J=0$ $K_a=0$	$\|1\ 0\ 0\ 0\rangle J=1$ $K_a=0$	180.660 95	0.177 63[a]
$\|0\ 0\ 1\ 0\rangle J=0$ $K_a=0$	$\|1\ 0\ 0\ 0\rangle J=1$ $K_a=1$	187.850 14	0.320 40[a]

[a]Excited initial state-intensity must be ratioed by Boltzmann weight. For a temperature of 5 K (typical of molecular beam experiments) the intensities for transitions originating from $|0\ 0\ 1\ 0\rangle J=0$ $K_a=0$ should be multiplied by 0.0103 and 0.1864 for $(HCl)_2$ and $(DCl)_2$, respectively. For a temperature of 140 K (typical of HCl cooled cell experiments) the intensities for transitions originating from $|0\ 0\ 1\ 0\rangle J=0$ $K_a=0$ should be multiplied by 0.8492 and 0.9418 for $(HCl)_2$ and $(DCl)_2$, respectively.

TABLE XI. Comparison of potential surfaces (ϕ fixed at 180°).

	E (cm^{-1})[a]	R (Å)	θ_1 (deg)	θ_2 (deg)
Latajka *et al.* *ab initio*[b]				
minimum	−555	3.838	11.3	89.7
barrier	45	3.740	50.6	129.4
Karpfen *et al.* *ab initio*[c]				
minimum	−602	3.912	6.60	88.93
barrier	71	3.856	47.23	132.77
Bunker *et al.*[d] analytical fit to Karpfen *et al.* *ab initio*				
minimum	−626	3.820	7.4	87.7
barrier	64	3.807	47.2	132.8
Votava *et al.* expanded semiempirical[c]				
minimum	−740	3.700	5	80.8
barrier	188	3.725	52	128.7
ES1				
minimum	−692	3.746	9	89.8
barrier	48	3.650	47	133

[a]Barrier energies relative to minimum.
[b]Reference 31.
[c]Reference 37.
[d]Reference 38.
[e]Reference 35.

analytical *ab initio* barrier of Bunker *et al.*[51] and the center of mass separation only contracts by about 0.1 Å as $(HCl)_2$ moves from the global minimum to the C_{2h} barrier geometry, these features are crucial in order to accurately reproduce the measured spectroscopic observables. The Bunker *et al.* analytical *ab initio* potential shows only a 0.013 Å radial contraction along this coordinate, but it should be noted that the directly obtained *ab initio* points[50] (which were fitted to the analytical form) at the minimum and the C_{2h} barrier indicate a larger contraction of 0.056 Å. This suggests that the accuracy of the analytical model itself could be a limiting factor in obtaining purely theoretical quantitatively correct potential surfaces for systems such as $(HCl)_2$, in addition to the usual problems associated with the limited accuracy of the *ab initio* methods. It is also interesting to note that the *ab initio* potential of Latajka *et al.*[44] precisely predicts a 0.1 Å contraction in R along the donor–acceptor interchange coordinate. None of the *ab initio* calculations, however, correctly predict the absolute magnitude of these center of mass distances.

The large variations in the experimental $J=0\rightarrow1$ energy differences for each vibrational state directly indicate the existence of strong angular–radial coupling. Indeed, this angular–radial coupling is responsible for the breakdown of the semirigid bender model (described in Paper I), which predicted a barrier of 20 cm^{-1} or less based on the experi-

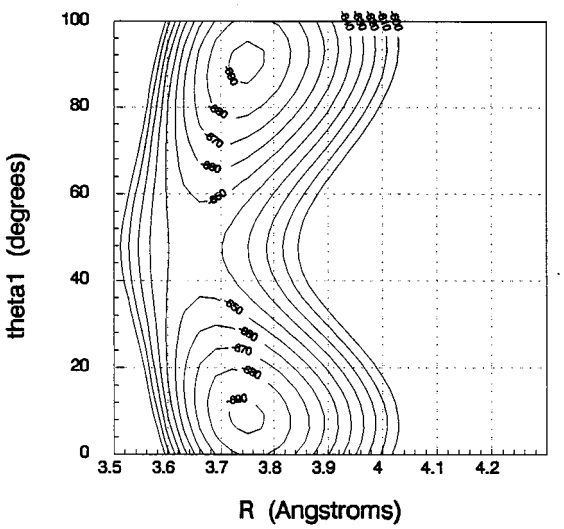

FIG. 5. Contour plot of ES1 potential showing radial dependence of donor–acceptor interchange tunneling pathway (other coordinates determined by energy minimization).

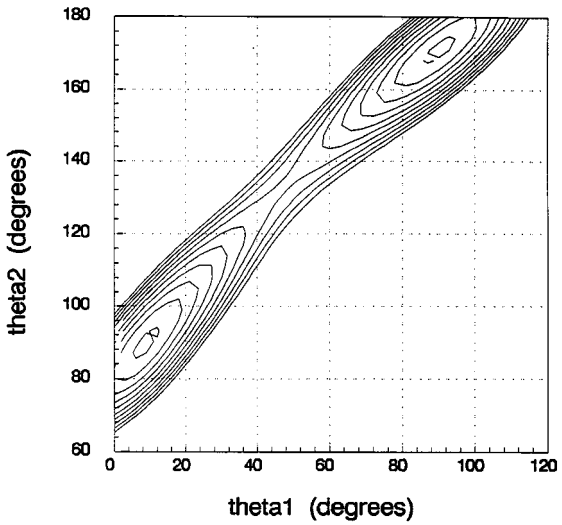

FIG. 4. Contour plot of ES1 potential. Contours from −690 to −590 cm^{-1} at 10 cm^{-1} intervals (other coordinates fixed at their equilibrium values).

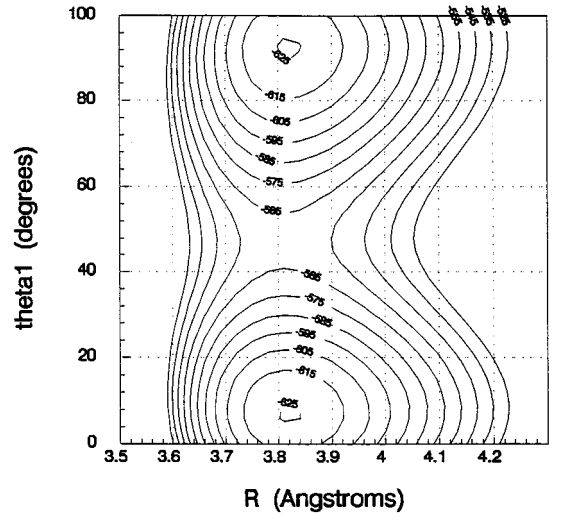

FIG. 6. Contour plot of *ab initio* potential showing radial dependence of donor–acceptor interchange tunneling pathway (other coordinates determined by energy minimization).

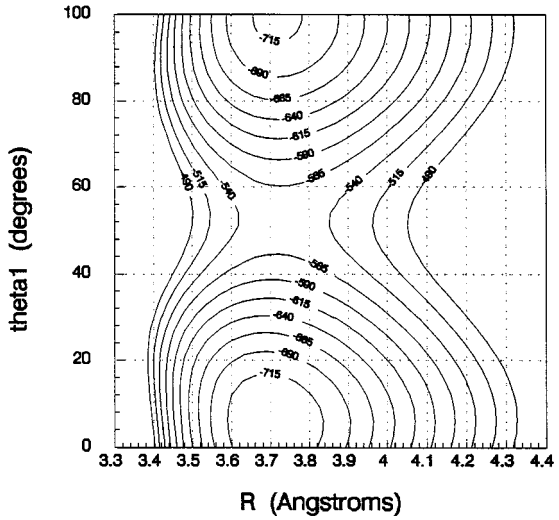

FIG. 7. Contour plot of Votava *et al.* potential showing radial dependence of donor–acceptor interchange tunneling pathway (other coordinates determined by energy minimization).

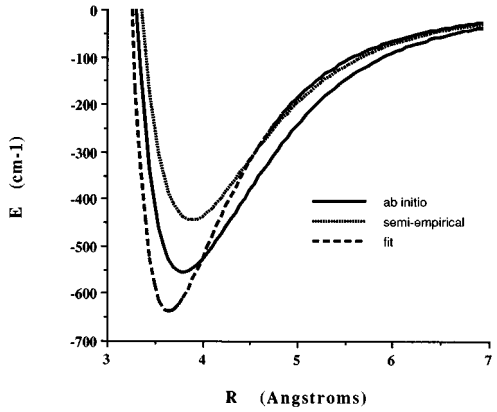

FIG. 9. Comparison of radial potentials with angles fixed at C_{2h} geometry.

mental ν_5 energy levels. Moreover, this finding quite graphically illustrates the inaccuracy of approximate angular (fixed R) calculations such as those utilized by Althorpe *et al.*[53] and Schuder *et al.*[37,38] which totally neglect angular–radial coupling. These results further suggest that as systems with less spherical symmetry than HCl are investigated, the errors due to the neglect of angular–radial coupling in approximate angular calculations are likely to render the information to be gained from such approximate approaches of questionable validity.

The two remaining intermolecular coordinates to be examined are the radial (R) and torsional (ϕ, out-of-plane) degrees of freedom. Because of the large amplitude donor–acceptor interchange dynamics occurring in the in-plane coordinates (θ_1 and θ_2), it is difficult to find a suitable graphical method to demonstrate the radial and torsional dependence of the potential. Therefore, we present one-dimensional plots for both R and ϕ with θ_1 and θ_2 fixed at both the global minimum geometry and the C_{2h} barrier geometry (Figs. 8–11) in order to provide a lower and upper limit for the effects due to the ''graphical'' in-plane averaging. For geometries with the in-plane angles fixed at the global minimum, the fitted radial potential closely matches the repulsive wall of the *ab initio* potential (as intended) while having a deeper well and shorter equilibrium intermolecular distance. The radial dependence of the ES1 potential more closely follows the Votava *et al.* potential at long range, which is encouraging since the latter potential was adjusted to reproduce the experimental low temperature second virial coefficients, which are sensitive to this region of the potential. The torsional dependence (ϕ) of the ES1 potential is steeper than the Bunker *et al. ab initio* potential, which is not surprising, considering that the out-of-plane bending frequency calculated from the *ab initio* surface was almost 25 cm^{-1} lower than the experimental value. The ES1 potential also reproduces the experimental combination frequency, $|0\ 0\ 1\ 1\rangle$, better than the *ab initio* surface indicating that the coupling between the in- and out-of-plane angular coordinates is much better described by the new potential.

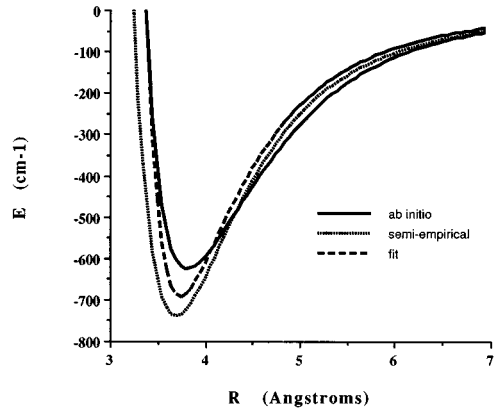

FIG. 8. Comparison of radial potentials with angles fixed at potential minimum.

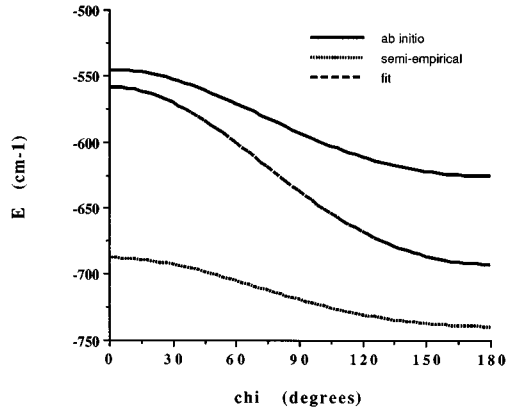

FIG. 10. Comparison of out-of-plane torsional (ϕ) potentials with angles fixed at potential minimum.

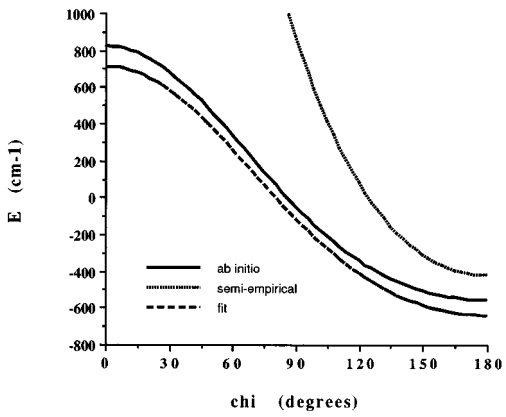

FIG. 11. Comparison of out-of-plane torsional (ϕ) potentials with angles fixed at C_{2h} geometry.

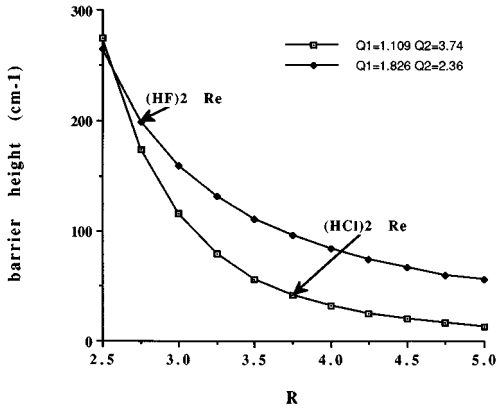

FIG. 12. Donor–acceptor interchange tunneling barrier height arising from dipole and quadrupole electrostatic forces for $(HF)_2$ and $(HCl)_2$ vs R.

X. ON THE NATURE OF HYDROGEN BONDING IN $(HCl)_2$

In recent years, the terms ''hydrogen bonding'' and ''electrostatic interactions'' have become virtually synonymous within the language of intermolecular forces. Because all of the classical hydrogen bonded systems—NH_3, H_2O, HF, and HCl—possess large multipole moments, this description ostensibly seems appropriate. Indeed, previous investigations of the HCl–HCl interaction have generally concluded that electrostatic forces are primarily responsible for the anisotropy of the potential energy surface at the radial minimum. However, the recently determined experimental IPS for the ArH_2O (Ref. 10) and $ArNH_3$ (Ref. 11) systems have provided reasons to question this simple view. At intermediate range, both the ArH_2O and $ArNH_3$ systems possess the linearly hydrogen bonded geometries dictated by the electrostatic induction (and dispersion) forces. However, as the radial minimum in the potential is approached, both the H_2O and NH_3 subunits rotate out of this hydrogen bonded geometry in order to minimize the rapidly varying anisotropic *repulsive* forces. Similar studies of the NH_3–NH_3 interaction also indicate that the repulsive forces can cause major modifications to the angular anisotropy at the radial minimum and that a linear hydrogen bonding geometry is obtained at slightly longer range.[70] This effect is surmised to lead to the near isoenergicity of the linear hydrogen bonded and cyclic conformations of $(NH_3)_2$ near the minimum in the IPS. Clearly, a closer inspection of the HCl–HCl interaction is warranted, given these precedents.

In agreement with *ab initio* calculations,[37] we find that the attractive forces are responsible for the slightly (9°) nonlinear hydrogen bond at the equilibrium separation. Although it is clear that the electrostatic forces are likewise responsible for the deep donor–acceptor interchange pathway, it is misleading to consider the electrostatic forces alone since the balancing repulsive forces are obviously required to achieve a stable equilibrium situation. Therefore, the magnitude of the electrostatic forces definitely depends at least parametrically on the repulsive forces. For example, the radial minimum for $(HCl)_2$ from the ES1 potential is 3.75 Å, while the radial minimum for $(HF)_2$ is about 2.75 Å,[30] indicating that the electrostatic forces near the minimum in $(HF)_2$ will be substantially larger than in $(HCl)_2$ due to the inverse R^n dependence in the electrostatic expressions, rather than simply due to the magnitudes of the electrostatic moments. Of course, the much longer equilibrium intermolecular separation for $(HCl)_2$ is due to the balance between the repulsion resulting from the more extended molecular orbitals of the HCl molecule and the sum of the attractive forces. In Fig. 12, we have plotted the donor–acceptor interchange tunneling barrier height as a function of R for two pure electrostatic surfaces characterized by the dipole and quadrupole moments of HF and HCl. An explanation for the much lower barrier height for $(HCl)_2$ as relative to that for $(HF)_2$ is based on the relative magnitudes of the relevant multipole moments. Although the HF multipole moments do favor a larger barrier, it is, however, actually the R dependence which ensures the much lower $(HCl)_2$ tunneling barrier. It should also be emphasized that for systems like $(HCl)_2$ with very small barriers that the higher electrostatic moments may play an important role.

Although electrostatic forces (as implicitly constrained by the balancing repulsive forces) undoubtedly play the dominant role in determining such topological features as the donor–acceptor interchange barrier in systems such as $(HF)_2$ and $(HCl)_2$, it is of interest to determine the degree to which the anisotropy of the repulsive forces themselves explicitly impact this problem. It is tempting to simply subtract the electrostatic contribution to the barrier height to determine the contribution from repulsion (the other attractive forces are very weakly anisotropic), however, this is not practical since the balance of forces is so precarious that relatively minor effects such as the influence of higher order electrostatic moments or the slight breakdown of the long-range electrostatic expressions themselves cannot be distinguished from genuine anisotropic repulsive effects. Because $(HF)_2$ possesses a much shorter equilibrium intermolecular separation, it is more obvious that anisotropic repulsive forces should have a major impact on the donor–acceptor interchange tunneling barrier. In fact, the *ab initio*[71] barrier for

$(HF)_2$ is found to be 332 cm^{-1}, while the simple electrostatic model depicted in Fig. 12 predicts a barrier of only about 200 cm^{-1}. However, it is also apparent that there is a fairly pronounced breakdown of the long-range electrostatic expressions at these short intermolecular distances, which complicates the $(HF)_2$ interpretation. Despite these difficulties, the new fitted $(HCl)_2$ potential surface *does* provide convincing evidence for the importance of anisotropic repulsive forces. The angular–radial coupling evident in the donor–acceptor interchange tunneling pathway cannot be reproduced by the mathematical form of the electrostatic expressions alone. Indeed, intuition would suggest that the reduced repulsive forces present at the C_{2h} geometry (where the hydrogen atom on one HCl molecule is as far as possible from both the hydrogen and chlorine atoms on the other HCl molecule) are actually responsible for the observed contraction of the intermolecular bond. These effects will undoubtedly be even more important in less spherical systems such as NH_3, H_2O, and HF. Therefore, fully rigorous dynamical treatments of these systems (with no assumptions involving the separability of the radial and angular degrees of freedom) will also be necessary in the prediction and fitting of high precision VRT data for the associated dimers.

The dominant influence of the electrostatic forces also ensures a stiff out-of-plane torsional barrier since both the dipole–quadrupole and quadrupole–quadrupole interactions demand planarity in order to maximize these attractive forces. The internal axis method (IAM) promoted by Hougen[72] to describe the donor–acceptor interchange tunneling problem in $(HF)_2$ holds only for planar tunneling paths. For $(HCl)_2$ this description should be quite accurate since the torsional barrier is much greater than the donor–acceptor interchange barrier. However, the increased effects of anisotropic repulsion expected for $(HF)_2$ could compromise this planar dynamical model.

XI. SUMMARY

We have described the first rigorous experimental determination of an intermolecular potential energy surface for a hydrogen bonded system. The $(HCl)_2$ surface was obtained by a direct least-squares fit of 8 parameters in a detailed analytical model to 33 spectroscopic observables for $(HCl)_2$ and $(DCl)_2$. We have employed a rigorous four-dimensional variational method to calculate the spectroscopic observables from the surface. Although the fitted surface confirms the preeminent role of the electrostatic forces in determining the topology of the potential surface, we find that anisotropic repulsive forces are crucial in rationalizing the radial dependence of the donor–acceptor interchange tunneling pathway. This potential surface will serve as a benchmark for testing simplified potential forms appropriate for condensed phase simulations, as well as for testing *ab initio* calculations. This work should provide useful insights for potential surface determinations for the other classical hydrogen bonded systems.

ACKNOWLEDGMENTS

The authors wish to thank Ron Cohen and Kun Liu for useful conversations, and Al van der Avoird for constructure criticism of the manuscript. Jeff Cruzan for help with graphics. This work was supported by the Experimental Physical Chemistry Program of the National Science Foundation (Grant No. CHE-9123335).

[1] R. J. Saykally and G. A. Blake, Science **259**, 1570 (1993).
[2] R. C. Cohen and R. J. Saykally, Annu. Rev. Phys. Chem. **42**, 381 (1991).
[3] J. M. Hutson, Annu. Rev. Phys. Chem. **41**, 123 (1990).
[4] *Inert Gases*, edited by R. A. Aziz (Springer, New York, 1984).
[5] S. Green, J. Chem. Phys. **96**, 4679 (1992).
[6] R. J. LeRoy and J. M. Hutson, J. Chem. Phys. **86**, 837 (1987).
[7] A. R. W. McKellar, J. Chem. Phys. **92**, 3261 (1990).
[8] J. M. Hutson, J. Phys. Chem. **96**, 4237 (1992); J. Chem. Phys. **96**, 6752 (1992).
[9] R. C. Cohen and R. J. Saykally, J. Chem. Phys. **98**, 6007 (1993).
[10] C. A. Schmuttenmaer, R. C. Cohen, and R. J. Saykally, J. Chem. Phys. **101**, 146 (1994).
[11] M. Quack and M. Suhm, J. Chem. Phys. **95**, 28 (1991).
[12] E. H. T. Olthof, A. van der Avoird, and P. E. S. Wormer, J. Chem. Phys. **101**, 8430 (1994).
[13] M. J. Elrod and R. J. Saykally, J. Chem. Phys. **103**, 921 (1995).
[14] R. H. Cole and S. Havriliak, Discuss. Faraday Soc. **23**, 13 (1957).
[15] J. G. Powles and M. Rhodes, Phys. Lett. A **24**, 523 (1967).
[16] H. Okama, N. Nakamura, and H. Chihara, J. Phys. Soc. Jpn. **24**, 452 (1967).
[17] D. F. Hornig and W. E. Osberg, J. Chem. Phys. **23**, 662 (1965).
[18] R. Savoie and A. Anderson, J. Chem. Phys. **44**, 548 (1966).
[19] T. S. Sun and A. Anderson, Spectrosc. Lett. **4**, 377 (1971).
[20] R. Savoie and M. Pezolet, J. Chem. Phys. **50**, 2781 (1969).
[21] H. B. Friedrich and R. E. Carlson, J. Chem. Phys. **53**, 4441 (1970).
[22] M. Ito, M. Suzuki, and T. Yokoyama, J. Chem. Phys. **50**, 2949 (1969).
[23] C. H. Wang and P. A. Fleury, J. Chem. Phys. **53**, 2243 (1970).
[24] E. Sandor and R. F. C. Farrow, Nature **213**, 171 (1967).
[25] E. Sandor and R. F. C. Farrow, Nature **215**, 1265 (1967).
[26] E. Sandor and M. W. Johnson, Nature **217**, 541 (1968).
[27] A. K. Soper and P. A. Egelstaff, Mol. Phys. **42**, 399 (1981).
[28] D. H. Rank, B. S. Rao, and T. A. Wiggins, J. Chem. Phys. **37**, 2511 (1962).
[29] D. H. Rank, P. Sitaram, W. A. Glickman, and T. A. Wiggins, J. Chem. Phys. **39**, 2673 (1963).
[30] T. R. Dyke, B. J. Howard, and W. Klemperer, J. Chem. Phys. **56**, 2442 (1972).
[31] N. Ohashi and A. S. Pine, J. Chem. Phys. **81**, 73 (1984).
[32] A. Furlan, S. Wulfert, and S. Leutwyler, Chem. Phys. Lett. **153**, 291 (1988).
[33] G. A. Blake, K. L. Busarow, R. C. Cohen, K. B. Laughlin, Y. T. Lee, and R. J. Saykally, J. Chem. Phys. **89**, 6577 (1988).
[34] M. D. Schuder, C. M. Lovejoy, D. D. Nelson, Jr., and D. J. Nesbitt, J. Chem. Phys. **91**, 4418 (1989).
[35] G. A. Blake and R. E. Bumgarner, J. Chem. Phys. **91**, 7300 (1989).
[36] N. Moazzen-Ahmadi, A. R. W. McKellar, and J. W. C. Johns, J. Mol. Spectrosc. **138**, 282 (1989).
[37] M. D. Schuder, C. M. Lovejoy, R. Lascola, and D. J. Nesbitt, J. Chem. Phys. **99**, 4346 (1993).
[38] M. D. Schuder, D. D. Nelson, Jr., and D. J. Nesbitt, J. Chem. Phys. **99**, 5045 (1993).
[39] M. Allavena, B. Silvi, and J. Cipriani, J. Chem. Phys. **76**, 4573 (1982).
[40] P. Hobza and R. Zahradnik, Chem. Phys. Lett. **82**, 473 (1981).
[41] P. Hobza and J. Sauer, Theor. Chim. Acta **65**, 279 (1984).
[42] Y. Hannachi and B. Silvi, J. Mol. Struct. (Theochem) **200**, 483 (1989).
[43] M. J. Frisch, J. A. Pople, and J. DelBene, J. Phys. Chem. **89**, 3664 (1985).
[44] Z. Latajka and S. Scheiner, Chem. Phys. **122**, 413 (1988).
[45] J. DelBene and I. Shavitt, Intern. J. Quantum Chem. Symp. **23**, 445 (1989).
[46] I. R. McDonald, S. F. O'Shea, D. G. Bounds, and M. L. Klein, J. Chem. Phys. **72**, 5710 (1980).
[47] M. L. Klein and I. R. McDonald, Mol. Phys. **42**, 243 (1981).

[48] R. Votava, R. Ahlrichs, and A. Geiger, J. Chem. Phys. **78**, 6841 (1983).
[49] B. Schramm and U. Leuchs, Ber. Bunsenges. Phys. Chem. **83**, 847 (1979).
[50] A. Karpfen, P. R. Bunker, and P. Jensen, Chem. Phys. **149**, 299 (1991).
[51] P. R. Bunker, V. C. Epa, P. Jensen, and A. Karpfen, J. Mol. Spectrosc. **146**, 200 (1991).
[52] P. Jensen, M. D. Marshall, P. R. Bunker, and A. Karpfen, Chem. Phys. Lett. **187**, 594 (1991).
[53] S. C. Althorpe, D. C. Clary, and P. R. Bunker, Chem. Phys. Lett. **187**, 345 (1991).
[54] A. E. Barton and B. J. Howard, Faraday Discuss. Chem. Soc. **73**, 45 (1982).
[55] S. L. Holmgren, M. Waldman, and W. Klemperer, J. Chem. Phys. **67**, 4414 (1977).
[56] G. A. Blake, K. B. Laughlin, K. L. Busarow, R. C. Cohen, D. Gwo, C. A. Schmuttenmaer, D. W. Steyert, and R. J. Saykally, Rev. Sci. Instrum. **62**, 1693 (1991).
[57] G. A. Blake, K. B. Laughlin, K. L. Busarow, R. C. Cohen, D. Gwo, C. A. Schmuttenmaer, D. W. Steyert, and R. J. Saykally, Rev. Sci. Instrum. **62**, 1701 (1991).
[58] D. P. Shoemaker, C. W. Garland, and J. W. Nibler, *Experiments in Physical Chemistry*, 5th ed. (McGraw-Hill, New York, 1989).
[59] M. R. Keenan, D. B. Wozniak, and W. H. Flygare, J. Chem. Phys. **75**, 631 (1981).
[60] A. B. McCoy, Y. Hurwitz, and R. B. Gerber, J. Phys. Chem. **97**, 12516 (1993).
[61] A. S. Pine and B. J. Howard, J. Chem. Phys. **84**, 590 (1986).
[62] This work.
[63] W. H. Press, S. A. Teukolsky, W. T. Vetterling, and B. P. Flannery, *Numerical Recipes*, 2nd ed. (Cambridge University Press, Cambridge, 1992).
[64] A. D. Buckingham, Adv. Chem. Phys. **12**, 107 (1967).
[65] J. O. Hirschfelder, C. F. Curtis, and R. B. Bird, *Molecular Theory of Gases and Liquids* (Wiley, New York, 1954).
[66] A. Kumar and W. J. Meath, Mol. Phys. **54**, 823 (1985).
[67] G. C. M. van der Sanden, P. E. S. Wormer, A. van der Avoird, C. A. Schmuttenmaer, and R. J. Saykally, Chem. Phys. Lett. **226**, 22 (1994).
[68] M. D. Schuder and D. J. Nesbitt, J. Chem. Phys. **100**, 7250 (1994).
[69] A. R. W. McKellar (private communication)
[70] A. van der Avoird, Faraday Discuss. Chem. Soc. **97**, (1994).
[71] P. R. Bunker, P. Jensen, A. Karpfen, M. Kofranek, and H. Lischka, J. Chem. Phys. **92**, 7432 (1990).
[72] J. T. Hougen and N. Ohashi, J. Mol. Spectrosc. **109**, 134 (1985).